AN ABSTRACT OF THE THESIS OF

Yu-Wei Su for the degree of Master of Science in Chemical Engineering presented on September 10, 2007.

Title: Fabrication and Characterization of Ferrimagnetic Film for RF/Microwave Crosstalk Suppression

Abstract approved:

Chih-Hung Chang

The primary goal of this thesis is to fabricate a magnetic film between the coplanar transmitted stripline for crosstalk suppression. Crosstalk is caused from undesired inductive and capacitive coupling of signals between two conductors. The effective crosstalk suppression results from the inductive coupling of circuit elements through the lossy properties of magnetic material during ferromagnetic resonance (FMR). Several techniques were used to fabricate ferrite films, including ferrite plating, screen printing, and pressure die casting. Ferrite plating produce nanostructured zinc iron oxide ($ZnFe_2O_4$) films with lower crystallinity and do not exhibit cross talk suppression. Interesting, the films show a higher roughness with increasing film thickness. The contact angle measurement indicates the films changing from hydrophobic to hydrophilic with increasing film thickness. Screen printing was used to fabricate yttrium iron garnet ($Y_3Fe_5O_{12}$) films to replace ferrite plating zinc ferrite films, because of the magnetic properties

of yttrium iron garnet film. The results show that screen-printed films can achieve far-end crosstalk suppression by 10 ~ 12dB, however, no suppression effect for near-end crosstalk. It is believed that the polymeric binder caused the problem. A pressure die casting technique was used to fabricate the yttrium iron garnet films. These films achieve the far-end crosstalk by 22dB and the near-end crosstalk by 8dB at higher frequency 3.75GHz. For G-113 and TTVG-1600 screen-printed films, the resonant frequency occurs at about 0.75GHz. For TTVG-1850 screen-printed and pressure casting film, the resonant frequency occurs at about 1.7GHz and 1.25GHz respectively. Finally, a new fabrication technique that combines continuous flow reactor for the generation of nanoparticle precursors and pressure die casting were proposed for making denser ferrite thin films.

Fabrication and Characterization of Ferrimagnetic Film for RF/Microwave Crosstalk Suppression

by
Yu-Wei Su

A THESIS

submitted to

Oregon State University

in partial fulfillment of
the requirements for the
degree of

Master of Science

Presented September 10, 2007
Commencement June 2008

Master of Science thesis of Yu-Wei Su presented on September 10, 2007.

APPROVED:

Major Professor, representing Chemical Engineering

Head of the School of Chemical, Biological & Environmental Engineering

Dean of the Graduate School

I understand that my thesis will become part of the permanent collection of Oregon State University libraries. My signature below authorizes release of my thesis to any reader upon request.

Yu-Wei Su, Author

ACKNOWLEDGEMENTS

I like to express my sincere gratitude and heartfelt appreciation to Dr. Chih-Hung Chang and Dr. Raghu Settaluri for their enormous support and invaluable guidance for this project. I am greatly indebted to Dr. Chang for his stimulating suggestions and kind words of encouragement that helped me tremendously through this research project and during the writing of this thesis. I would always be grateful to him for having shown me this way and for providing an opportunity to work with him on this wonderful project which is supported by the National Science Foundation's Electronics, Photonics & Device Technologies's program under grant # ECS-0401357 and Process & Reaction Engineering program under a CAREER grant # CTS-0348723.

I would also like to extend my appreciation to my committee members: Dr. Gregory L. Rorrer, Dr. Raghu Settaluri, and Dr. Kaichang Li for their time and commitment to my M.S program.

For the device testing, I would like to thank Dr. Raghu Settaluri and Dr. Andreas Weisshaar from Electrical Engineering for opening their microwave testing laboratory and sharing their expertise, and Arien Sligar, Eric Vernon for teaching me basic RF/Microwave knowledge.

I like to thank Chih-Heng Tseng from the Industrial and Manufacturing Engineering for his assistance in operating pressmaster vaccum press and Nd:YAG pulsed laser machining tool, Chien-Chih Huang and Seungwha Kown from the Mechanical Engineering for providing vibratory mill machine. I would like to

thank all of my labmates Yu-Jen Chang, Jiqing Hu, Doo-Hung Lee, Shuhong Liu, Hyung Dae Jim, Seungyeol Han, and Wei Wang for their academic assistance, and all others who ever helped me.

Finally, I like to dedicate my most special thanks to my loving parents for their financial and spiritual support.

TABLE OF CONTENTS

TABLE OF CONTENTS (Continued)

LIST OF FIGURES

LIST OF FIGURES (Continued)

LIST OF TABLES

Alternative Fabrication of Ferrimagnetic Film on RF/Microwave Crosstalk Suppression

CHAPTER 1

Introduction

With the increasing demand for advanced wireless communication, mixed-signal integrated circuits (ICs) and system-on-chip (SOC) approaches have attracted lots of attention, due to their ability to reduce overall chip size. Electromagnetic noise was introduced into the circuit from nearby components leading to unwanted electrical response deviation. Crosstalk is apparently observed in transmission line, which can be in the form of coaxial line, microstrip lines and coplanar waveguide (CPW). Due to the close proximity of the conductors, the electric and magnetic fields generated by different lines interact, giving rise to electro-magnetic coupling between the transmission line. The electro-magnetic coupling also causes mutual capacitance and inductance, which has coupling of signals and will result unwanted noise between two closely spaced lines. If the unwanted noise becomes large enough, it degrades the performance of a circuit. With feature size decreasing, it is essential for efficient crosstalk suppression.

Several methods, including differential signaling [1], guard traces [2], and substrate compensation, are recently available to crosstalk suppression. The differential signaling method is applying a new twisted differential line (TDL) to reduce crosstalk. The structure is comprised of two-segmented conductor traces, crisscrossing each other by many vias on a first and second layer of the PCB [1].

Guard traces are typically used in a microstrip or stripline environment, where the grounded guard conductor is placed between two circuit elements as shown in Figure 1.1. A row of closely spaced metal vias are placed connecting the top and bottom ground planes for the purpose of suppressing parallel plate waveguide mode propagation. Crosstalk as a result of inductive coupling can be reduced by grounding both ends of the guard trace. Although this method works well for crosstalk suppression, an additional coupling mode will be introduced and cause the crosstalk to increase, if no minimum spacing between the guard trace and circuit elements is maintained [2].

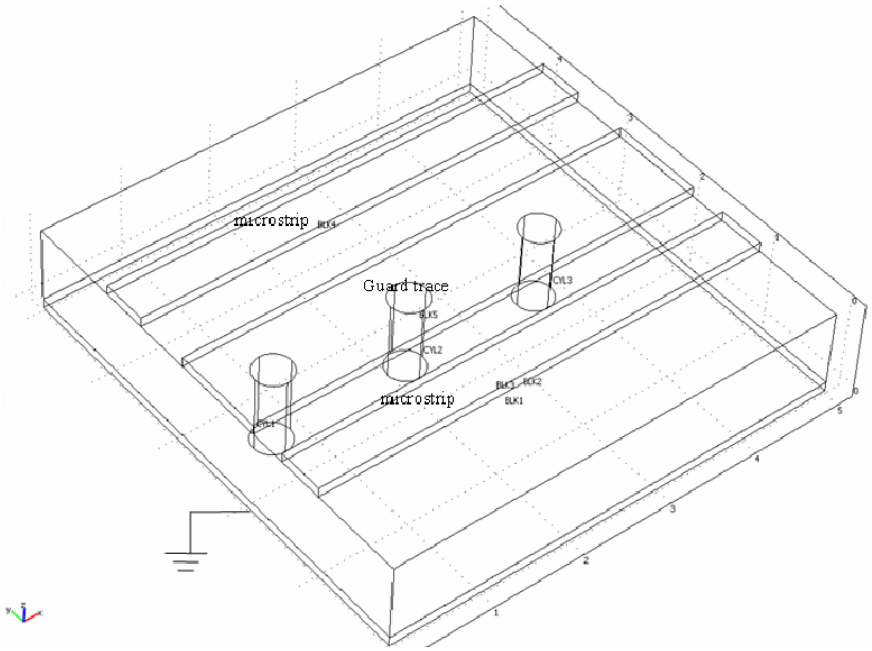

Figure 1.1 The schematic diagram of crosstalk suppression with the use of a guard trace with vias to ground, implanted in microship configuration.

Another method for reducing crosstalk is to apply substrate compensation [3]. A substrate (Figure 1.2) with two layers of different dielectric constants is used to eliminate the far-end crosstalk, but only far-end crosstalk has effective reduction.

Near-end crosstalk still is not apparently reduced. One major limitation for this method is the complicated fabrication of multilayer dielectric substrate.

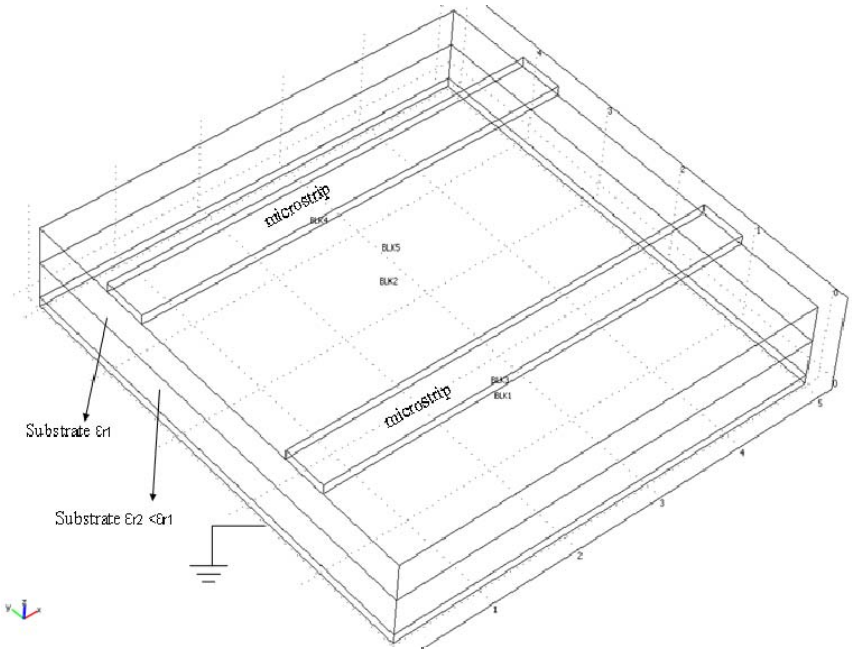

Figure 1.2 The schematic diagram of the multilayered substrate, which is used to suppress crosstalk through substrate compensation.

Based on above consideration, the approach presented here for reducing crosstalk is to fabricate the magnetic film in the area separating two closely spaced microstrips. This effective crosstalk suppression results from the inductive coupling of circuit elements through the lossy properties of magnetic material during ferromagnetic resonance (FMR). Prior research reported application of magnetic films on the circuit device to prevent radiation of high frequency noise [4~10]. Therefore, the fabrication of magnetic films plays an important role on circuit design aspect for noise suppression. This thesis covers the fabrication and surface properties of zinc ferrite film, using ferrite plating. For crosstalk suppression measurement, screen printing and pressure die casting techniques are

used to fabricate YIG (yttrium iron garnet: $Y_3Fe_5O_{12}$) magnetic films instead of previous zinc ferrite film. Finally, a new fabrication technique employing a continuous flow reactor system is proposed to synthesize nanoparticles, to be enhanced for ferrite magnetic film, and then for crosstalk suppression.

CHAPTER 2

Literature Review

2.1 Magnetic Film on Application of Crosstalk Suppression

Many reported references focused on using magnetic film with different dimensions on transmission line to observe the noise suppression effect. The amorphous magnetic films composed of $Co_{85}Nb_{12}Zr_3$ were made by RF magnetron sputtering on polyimide layer. Masahiro Yamaguchi applied simulation and experiment on the dimensional effect for RF noise suppression. The magnetic films directly cover on top of the coplanar transmission line. Yamaguchi's group analyzed the power loss versus frequency by using the commercial simulation software (HFSS) with finite element analying function [11]. The simulation result shows that RF noise suppression by soft magnetic films are apparently as a function of the width (50 ~ 2000μm) and thickness (0.1, 0.3, 0.5, and 1μm). As decreasing the width and increasing the thickness of the magnetic film, the FMR frequency is shifted to higher frequency because of various values of demagnetization factors, N_x, N_y, and N_z. In addition to CoNbZr magnetic films, CoPdAlO [12] and CoZrO [13] films are also studied for the noise suppression effect by measuring transmission parameter (S_{21}) and reflection parameter (S_{11}) under microwave frequency. The main goal of this technique is to eliminate the radiation of high frequency noise by increasing the insertion loss in the stop band, where signals need to be attenuated. This method is not particularly suitable for

crosstalk suppression due to high insertion loss when a magnetic film is placed directly on top of the transmission line.

2.2 Magnetic Material

2.2.1 Classification of Magnetic Material

The magnetism of all bulk materials can be classified as five categories (Table 2.1), diamagnetism, paramagnetism, ferromagnetism, antiferromagnetism, and ferrimagnetism. The susceptibility is a parameter that demonstrates how responsive a material is to an applied magnetic field. It is expressed by the ratio of magnetization (M) and magnetic field (H).

$$\chi = \frac{M}{H} \qquad [2.1]$$

Diamagnetic materials have the atom without net magnetic moment under zero applied fields. Under the influence of an applied field (H), the spinning electrons precess, and then this kind of motion, which is a type of electric current, produces a magnetization (M) in the opposite direction to that of the applied field.

Paramagnetic materials have the atoms with randomly oriented magnetic moments. The application of a magnetic field creates a slight alignment of these moments, and then causes a low magnetization in the same direction as the applied field. As the temperature increases, the susceptibility will decrease because the thermal agitation causes the atomic magnetic moments difficultly to align. Therefore, the susceptibility is strongly a temperature dependant parameter.

Ferromagnetic materials have parallel-aligned magnetic moments in a lattice, and have a large and positive susceptibility to an external magnetic field. In the

periodic table, only Fe, Co and Ni have ferromagnetism below a Curie temperature (T_c). In 1907, Weiss postulated the presence of magnetic domains within the material, which are regions where the atomic magnetic moments are aligned. Under applied field, the movement of these domains determines how the material responds to a magnetic field, and as a consequence the susceptible is a function of applied magnetic field. The typical phenomenon for ferromagnetic material is the hysteresis loop. Hysteresis loop is a non-linear initial magnetization curve, as the changing magnetization with applied field due to a change in the magnetic domain structure, which is composed of several dipole moments. The more domains that are aligned, the stronger the magnetization exists in the material. Until all domains are aligned, the material is magnetically saturated. In this situation, no additional amount of external magnetic force will cause an increase in its internal magnetization. The reason for the presence of saturation magnetization (M_s) is on completely orientated domains.

In the periodic table, chromium is the only element exhibiting anti-ferromagnetism at room temperature. Anti-ferromagnetic materials are very similar to ferromagnetic materials but the exchange interaction between neighboring atoms leads to the anti-parallel alignment of the atomic magnetic moments. Therefore, the magnetic field cancels out and the material appears to behave in the same way as a paramagnetic material.

Ferrimagnetic materials are of great technical importance due to the presence of spontaneous magnetic moment and hysteresis phenomenon below a Curie

temperature, just as iron, cobalt, or nickel. In other words, much like ferromagnetic, ferrimagnetic material posses small domains in which the electron spins are spontaneously aligned in parallel. The main difference from ferromagnetism is that ferrimagnetism is only observed in oxide ceramic compounds. These examples include the ferrite compound ($MO{\cdot}Fe_2O_3$, M=Ba, Ni, Zn) and the iron garnet compound ($A_3B_2(FeO_4)_3$, A=Y, Ca, V, B=Fe). Within these materials the exchange interactions lead to parallel alignment of atoms in some of the crystal sites and anti-parallel alignment of others. It can be clearly noticed from the second column of Table 2.1 that ferrimagnetism contains similar parallel atomic behaviors as ferromagnetism and anti-ferromagnetism. This causes some of the magnetic moments to remain uncancelled, resulting in a net magnetic moment exists. Thus, ferrimagnetic material can be viewed as imperfect anti-ferromagnetics.

Type of magnetism	Atomic behavior	Magnetic behavior	Example	Susceptibility: χ (c.g.s unitless)
Diamagnetism		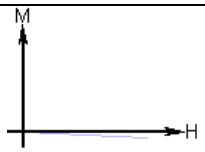	Au	$-2.74*10^{-6}$
			Cu	$-0.77*10^{-6}$
Paramagnetism	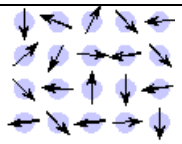	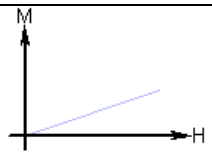	β-Sn	$0.19*10^{-6}$
			Pt	$21.04*10^{-6}$
			Mn	$66.10*10^{-6}$
Ferromagnetism	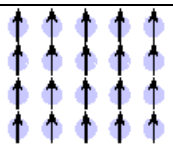	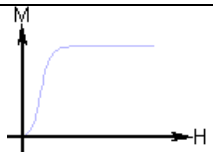	Fe	$10^{2\sim}10^{4}$
Antiferromagnetism	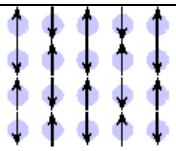	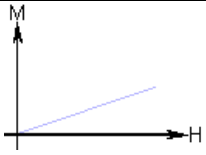	Cr	$3.6*10^{-6}$
Ferrimagnetism	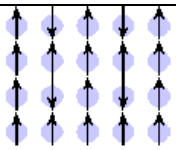	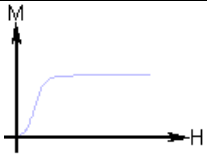	Ba Ferrite	~3

Table 2.1 Summary of different types of magnetic behavior [14]

2.2.2 Zinc Ferrite

The spinel ferrite (MFe_2O_4, M=Zn, Mn, and Ni) is an ideal material system for high frequency passive components because of its high permeability, resistivity and permittivity. Ferrites with the spinel structure include normal spinel $M[Fe_2]O_4$, where M as Zn, Cd, and Ca and inverse spinel $Fe[MFe]O_4$ where M as Ni, Co, Mn, Cu. For example, $ZnFe_2O_4$ has normal spinel crystal structure (Figure 2.2) possesses the space group *fd3m* and consists of 56 atoms; 32 oxygen anions (blue), 8 Zn^{2+} cations (A: green) residing on tetrahedral sites, and 16 Fe^{3+} cations (B: red) residing on octahedral sites [14]. The size and valence of the cation species determine the filling of these sites and strongly influence the material's magnetic and electronic properties.

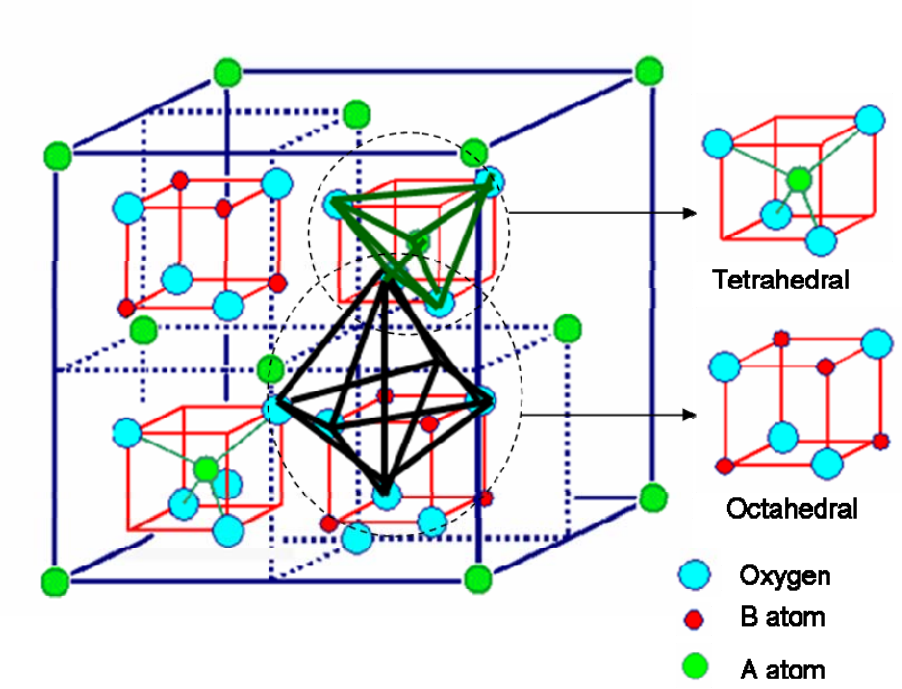

Figure 2.1 Normal spinel crystal structure of Zinc Ferrite.

2.2.3 Yttrium Iron Garnet

Yttrium iron garnet (YIG), with the chemical composition $Y_3Fe_2(FeO_4)_3$, is one of the general garnet compound ($A_3B_2^{'}B_3^{''}O_{12}$), where A, $B^{'}$, and $B^{''}$ are metal ions occupying different symmetry sites. It has a body center cubic structure with 160 atoms in the cubic cell. The space group is classified as "Ia3d" or "O_h^{10}". Ferrimagnetisms is only observed in compounds, which have more complex crystal structures than pure elements. Within these materials the exchange interactions lead to parallel alignment of atoms in some of the crystal sites and anti-parallel alignment of others. The material breaks down into magnetic domains, just like a ferromagnetic material. Magnetic behavior is also very similar, although ferrimagnetic materials usually have lower saturation magnetizations.

The crystal structure of YIG (Figure 2.1) has two different sites for iron ions. Fe^{3+}_{oct} (B' ions) occupy the 16 sites with an octahedral symmetry, and Fe^{3+}_{tet} ($B^{''}$ ions) occupy the 24 sites with a tetrahedral symmetry. Fe^{3+}_{oct} ions and Fe^{3+}_{tet} ions are represented by purple octahedrons and deep blue tetrahedrons respectively. Yttrium (Y^{3+}) ions represented by light blue balls occupy the 24 sites and each is dodecahedrally coordinated to eight oxygen ions shared with an octahedron and a tetrahedron. Oxygen ions occupy 96 sites. Due to the opposing spin electrons of Fe^{3+}_{oct} and Fe^{3+}_{tet} ions, YIG exhibits ferrimagnetic behavior. One important application of the garnet material is on microwave ferrite devices by substituting A, $B^{'}$, and $B^{''}$ sites with rare earth elements, because of its very narrow ferromagnetic resonance line width.

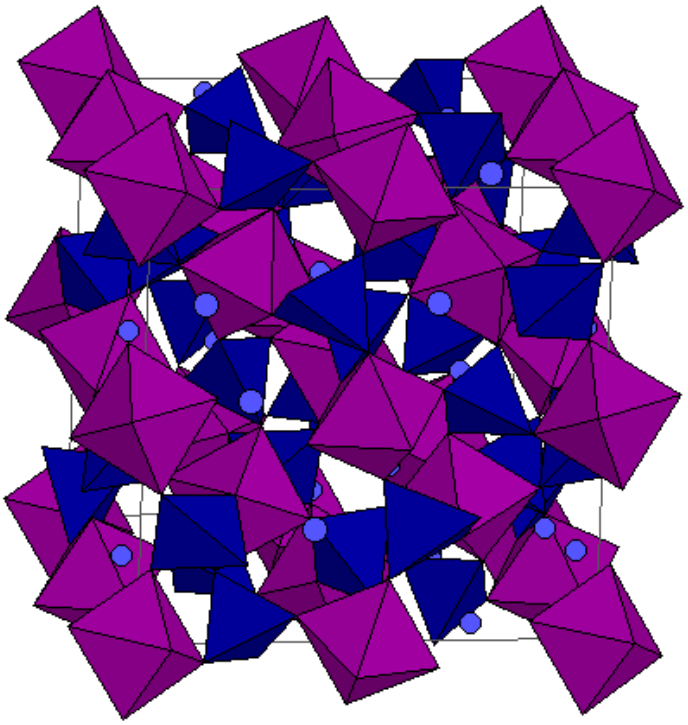

Figure 2.2 Crystal structure of YIG.

2.3 Ferromagnetic Resonance

2.3.1 Introduction

Ferromagnetic resonance (FMR) was discovered by Russian physicist, V. K. Arkad'yev, when he observed the absorption of ultra high frequency (UHF) radiation by ferromagnetic materials in 1911. For the application of magnetization, FMR is a spectroscopic technique to probe spin waves and spin dynamics of ferromagnetic materials. FMR is very similar to nuclear magnetic resonance (NMR) except FMR probes the magnetic moment of electrons and NMR probes the magnetic moment of the proton. Ferromagnetic resonance is known as the strong interaction between the magnetic moment of a magnetic dipole and an applied alternating magnetic field. When an external static magnetic field is applied to the single dipole, a precession about the axis of the applied field occurs in the direction shown in Figure 2.3(a). The magnetic field puts a torque on the magnetization which causes the magnetic moment to presses. In the absence of radio-frequency (RF) magnetic pumping field to sustain this precession, the rotation will not keep precessing and eventually spiral into alignment with the direction of the static magnetic axis. The phenomenon is shown in Figure 2.3(b). With applying an RF magnetic field in the plane normal to the static applied field, a pumping action can occur to maintain the precession of the magnetic dipoles, shown in Figure 2.3(c). This RF applied field will have the strongest interaction with the magnetic dipoles when its frequency is at resonant frequency (ω_r). The

interaction between RF and magnetic field dipoles cause high energy adsorption of the magnetic field in the form of radiated heat.

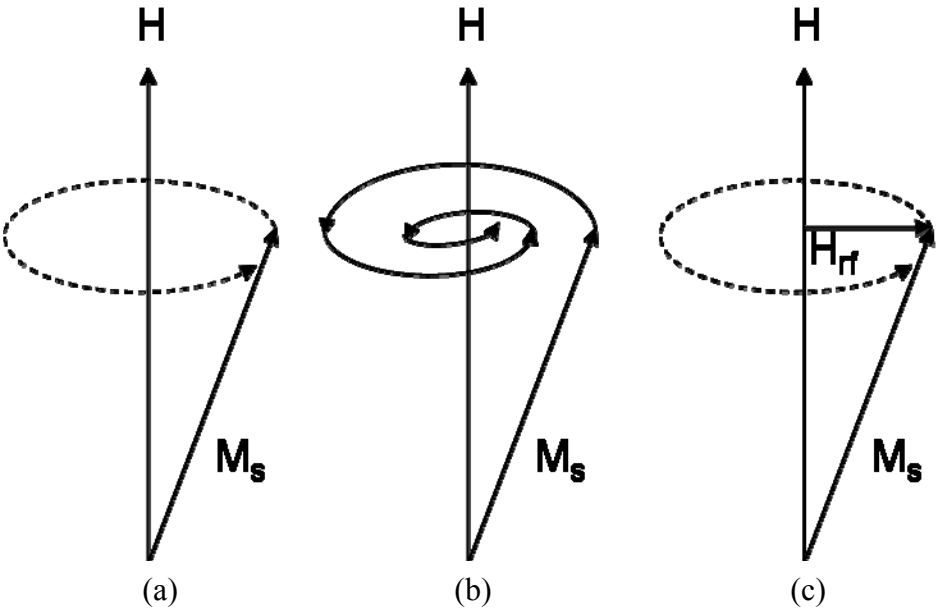

Figure 2.3 (a) The precession of a magnetic dipole caused by the external magnetic field without any loss. (b) Friction loss causes magnetic dipole to align with the external magnetic field. (c) An RF magnetic field causes the magnetic dipole precess along the axis of external magnetic field. [15]

2.3.2 Basic Properties of Ferrimagnetic Materials

The frequency in which the dipole rotates in a finite shape has been discussed in detail by Charles Kittel [16]. Much mathematics is involved in explaining the theory of ferromagnetic resonance [17]. In this section, the derivation of resonant frequency is briefly discussed in SI units as follows.

Considering a ferrite sample placed in the magnetic field (Figure 2.4), the internal field, H_0, to a ferrite sample is generally different from the externally applied field H_a, because of the boundary conditions at the surface of ferrite.

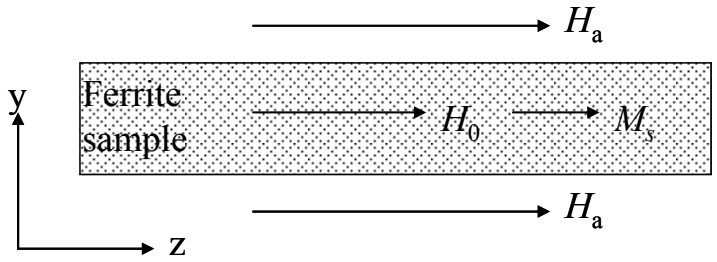

Figure 2.4 Tangential biased internal and external fields for a thin ferrite plate.

Therefore, the relationship between internal and external fields is given in equation [2.2].

$$H_0 = H_a - M_s \qquad [2.2]$$

The internal field, $\vec{H}$, is affected by the shape of the ferrite sample and its orientation with respect to the external field, $\vec{H}_e$, and can be expressed analogously as

$$\vec{H} = \vec{H}_e - N\vec{M} \qquad [2.3]$$

where $N = N_x$, N_y or N_z is called the demagnetization factors for the direction of the external field. For a z-biased ferrite with transverse RF field, equation [2.3] reduces to

$$H_x = H_{xe} - N_x M_x \qquad [2.4a]$$

$$H_y = H_{ye} - N_y M_y \qquad [2.4b]$$

$$H_z = H_a - N_z M_s \qquad [2.4c]$$

where H_{xe}, H_{ye} are the RF fields external to the ferrite, and H_a is the externally applied bias field. M_x and M_y, are the magnetization along x, y axis. M_s is the saturation magnetization along z axis. If the AC $\vec{H}$ field has $e^{j\omega t}$ time harmonic dependence, $\vec{H}$ and $\vec{M}$ have the linear relationship in [2.5].

$$\begin{bmatrix} M_x \\ M_y \\ M_z \end{bmatrix} = \begin{bmatrix} \chi_{xx} & \chi_{xy} & 0 \\ \chi_{yx} & \chi_{yy} & 0 \\ 0 & 0 & 0 \end{bmatrix} \begin{bmatrix} H_x \\ H_y \\ H_z \end{bmatrix} \qquad [2.5]$$

where the elements of susceptibility tensor [χ] are given by equation [2.6a, b].

$$\chi_{xx} = \chi_{yy} = \frac{\omega_0 \omega_m}{\omega_0^2 - \omega^2} \qquad [2.6a]$$

$$\chi_{xy} = -\chi_{yx} = \frac{j\omega\omega_m}{\omega_0^2 - \omega^2} \qquad [2.6b]$$

where

$$\omega_0 = \mu_0 \gamma H_0 = \mu_0 \gamma H_z = \mu_0 \gamma (H_a - N_z M_s) \qquad [2.7]$$

$$\omega_m = \mu_0 \gamma M_s \qquad [2.8]$$

γ is the gyromagnetic ratio (Appendix A), which is the ratio of magnetic moment and angular momentum. μ_0 (4π*10^{-7} H/m) is the free space permeability. From [2.5], M_x and M_y can be written as equation [2.9a, b].

$$M_x = \chi_{xx} H_x + \chi_{xy} H_y \qquad [2.9a]$$

$$M_y = \chi_{yx} H_x + \chi_{yy} H_y \qquad [2.9b]$$

Substituting [2.4a, b] into [2.9a, b] to eliminate H_x and H_y gives

$$M_x = \chi_{xx} H_{xe} + \chi_{xy} H_{ye} - \chi_{xx} N_x M_x - \chi_{xy} N_y H_y \qquad [2.10a]$$

$$M_y = \chi_{yx} H_{xe} + \chi_{yy} H_{ye} - \chi_{yx} N_x M_x - \chi_{yy} N_y H_y \qquad [2.10b]$$

These equations can be solved for M_x, M_y to give

$$M_x = \frac{\chi_{xx}(1+\chi_{yy}N_y) - \chi_{xy}\chi_{yx}N_y}{D} H_{xe} + \frac{\chi_{xy}}{D} H_{ye} \qquad [2.11a]$$

$$M_y = \frac{\chi_{yx}}{D} H_{xe} + \frac{\chi_{yy}(1+\chi_{xx}N_x) - \chi_{yx}\chi_{xy}N_x}{D} H_{ye} \qquad [2.11b]$$

where $$D = (1+\chi_{xx}N_x)(1+\chi_{yy}N_y) - \chi_{yx}\chi_{xy}N_xN_y \qquad [2.12]$$

For a finite-sized ferrite sample the gyromagnetic resonance frequency is altered by the demagnetization factors, and give by the condition D = 0 in [2.11]. Substituting [2.6a, b] into [2.12] and setting the result equal to zero gives

$$\left(1+\frac{\omega_0\omega_m N_x}{\omega_0^2-\omega^2}\right)\left(1+\frac{\omega_0\omega_m N_y}{\omega_0^2-\omega^2}\right) - \frac{\omega^2\omega_m^2 N_xN_y}{(\omega_0^2-\omega^2)^2} = 0 \qquad [2.13]$$

After rearrangement, this result can be reduced to give the resonance frequency, ω_r as

$$\omega_r = \omega = \sqrt{\left(\omega_0 + \omega_m N_x\right)\left(\omega_0 + \omega_m N_y\right)} \qquad [2.14]$$

Appling [2.7], [2.8] into [2.14], and then the resonant frequency, f_r (Hz), can be written in [2.15] instead of resonant angular frequency ω_r (rad/s).

$$f_r = \frac{\omega_r}{2\pi} = \frac{\mu_0 \gamma}{2\pi}\sqrt{\left[H_a + \left(N_x - N_z\right)M_s\right]\left[H_a + \left(N_y - N_z\right)M_s\right]} \qquad [2.15]$$

This is known as Kittel's equation, which can be used to predict ferromagnetic resonant frequency. In c.g.s system, H_a (Oersted, Oe) is the applied field and M_s is saturation magnetization, which is expressed as $4\pi M_s$ (Gauss, G). Other parameters, $\mu_0 = 1\,(\mathrm{G/Oe})$ is the free space permeability, and $\gamma/2\pi$ = 2.8(MHz/Oe) in Appendix A. Based on Kittel's equation, it is understood that the resonant frequency is affected by the shape and geometry of magnetic film, due to demagnetization factors. According to the coordination of the magnetic film, demagnetization factors, N_x, N_y and N_z, are defined in [2.16] to [2.18].

$$N_z = \frac{2t}{\pi L} \qquad [2.16]$$

$$N_y = \frac{2t}{\pi W} \qquad [2.17]$$

$$N_x = 1 - (N_z + N_y) \qquad [2.18]$$

These terms, t, L and W represent the thickness, length, and width of the magnetic film. Because t is much smaller than L and W, N_z and N_y approach zero; N_x is approximately to 1. Therefore, [2.15] becomes [2.19] by substituting the approximate values of demagnetization factors.

$$\omega_r = \mu_0 \gamma \sqrt{\left(H_a + M_s\right) H_a} \qquad [2.19]$$

Saturation magnetization also can be predict by

$$M_s = \frac{\omega_r^{\,2}}{\mu_0^{\,2} \gamma^2 H_a} - H_a \qquad [2.20]$$

For an infinite ferrite medium, Equations [2.6a, b] show that the elements of susceptibility tensor become infinite when the frequency, ω, equals the Larmor frequency, ω_0. This effect is known as gyromagnetic resonance, and occurs when the forced precession frequency is equal to the free precession frequency. All real ferrite materials have various magnetic loss mechanisms. As with other resonant system, loss can be accounted by making the resonant frequency in the complex form, $\omega_0 + j\alpha\omega$, where α is a damping factor. Substituting the complex resonant frequency into [2.6a, b] and makes the susceptibilities complex:

$$\chi_{xx} = \chi_{xx}^{'} - j\chi_{xx}^{''} \qquad [2.21a]$$

$$\chi_{xy} = \chi_{xy}^{''} + j\chi_{xy}^{'} \qquad [2.21b]$$

where the real and imaginary parts are given by

$$\chi'_{xx} = \frac{\omega_0 \omega_m \left[\omega_0^2 - \omega^2\left(1-\alpha^2\right)\right]}{\left[\omega_0^2 - \omega^2\left(1+\alpha^2\right)\right]^2 + 4\omega_0^2\omega^2\alpha^2} \qquad [2.22a]$$

$$\chi''_{xx} = \frac{\alpha\omega\omega_m \left[\omega_0^2 + \omega^2\left(1+\alpha^2\right)\right]}{\left[\omega_0^2 - \omega^2\left(1+\alpha^2\right)\right]^2 + 4\omega_0^2\omega^2\alpha^2} \qquad [2.22b]$$

$$\chi'_{xy} = \frac{\omega\omega_m \left[\omega_0^2 - \omega^2\left(1+\alpha^2\right)\right]}{\left[\omega_0^2 - \omega^2\left(1+\alpha^2\right)\right]^2 + 4\omega_0^2\omega^2\alpha^2} \qquad [2.22c]$$

$$\chi''_{xy} = \frac{2\omega_0\omega_m\omega^2\alpha}{\left[\omega_0^2 - \omega^2\left(1+\alpha^2\right)\right]^2 + 4\omega_0^2\omega^2\alpha^2} \qquad [2.22d]$$

For most ferrite materials, the loss is small, so $\alpha << 1$, and [2.22] can be sketched in Figure 2.5 based on some assumptions. It is assumed that α=0.05, ω_0=5, ω_m=1. The damping factor, α, is related to the linewidth, ΔH, of the susceptibility curve near resonance. Consider the plot of χ''_{xx} versus bias field H_0 at the resonant frequency ω_0, shown in Figure 2.6. At the fixed frequency, resonance occurs when $H_0 = H_r$, such that $\omega_0 = \mu_0\gamma_0 H_0$. Therefore, the x-axis can also be regarded as magnetic field H_0 because μ_0 and γ_0 both are constants. The unit conversion does not change the shape of the curve. The linewidth is defined as the width of the curve, where χ''_{xx} has decreased to half its peak value. If we assume $(1+\alpha^2)$ approximately equal to 1 and $\omega = \omega_0$, the peak value of χ''_{xx} in [2.22b] is $\frac{\omega_m}{2\omega_0\alpha}$.

Now let ω_{02} be the Larmor frequency for which $H_0 = H_2$, where χ''_{xx} has decreased to half its maximum value. Then we can solve [2.22b] to get [2.25].

$$\frac{1}{2}\chi_{xx}^{"} = \frac{\omega_m}{4\omega_0\alpha} = \frac{\alpha\omega_0\omega_m\left[\omega_{02}^2 + \omega_0^2\left(1+\alpha^2\right)\right]}{\left[\omega_{02}^2 - \omega_0^2\left(1+\alpha^2\right)\right]^2 + 4\omega_{02}^2\omega_0^2\alpha^2} \quad [2.23]$$

$$\Rightarrow 4\alpha^2\omega_0^4 = \left(\omega_{02}^2 - \omega_0^2\right)^2 \quad [2.24]$$

$$\Rightarrow \omega_{02} = \omega_0\sqrt{1+2\alpha} \simeq \omega_0\left(1+\alpha\right) \quad [2.25]$$

Then $\Delta\omega_0 = 2(\omega_{02} - \omega_0) \simeq 2\alpha\omega_0$, and using $\omega_0 = \mu_0\gamma_0 H_0$ gives the linewidth as

$$\Delta H = \frac{\Delta\omega_0}{\mu_0\gamma} = \frac{2\alpha\omega_0}{\mu_0\gamma} \quad [2.26]$$

From [2.26], it is very clear to understand that smaller damping factor causes the narrower linewidth.

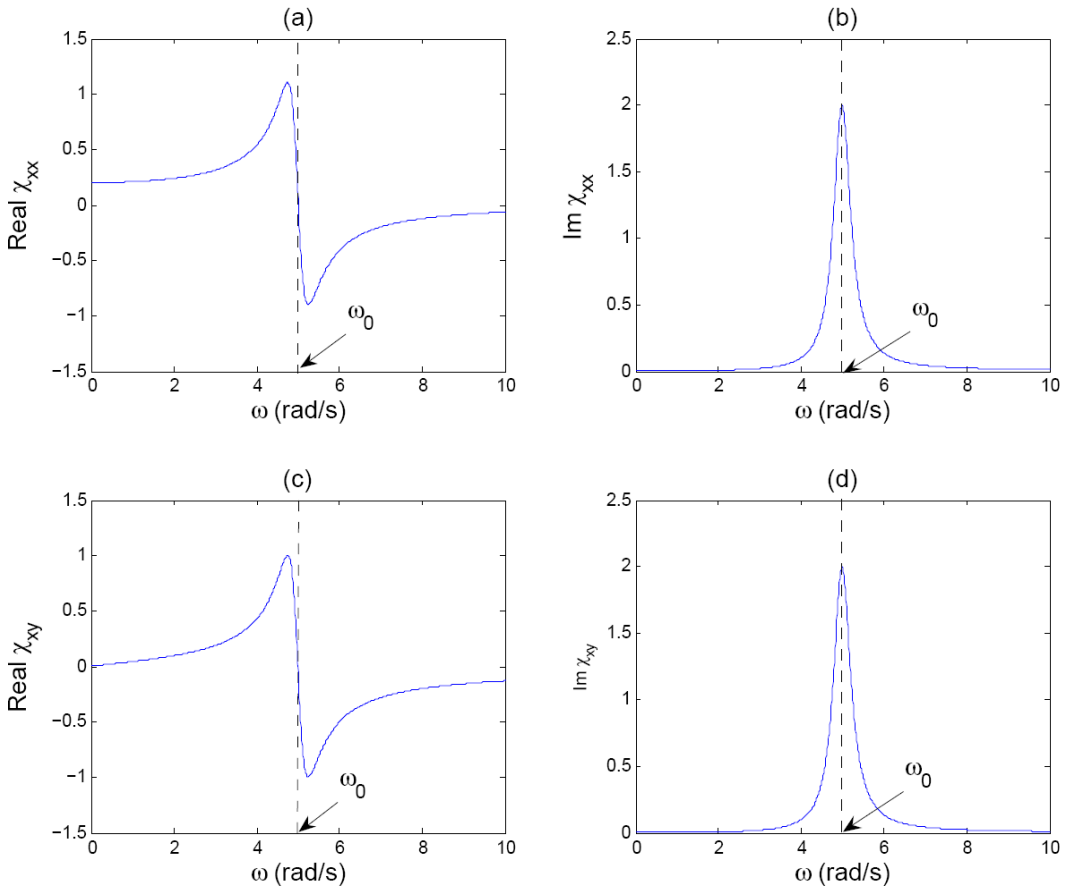

Figure 2.5 Complex susceptibilities for a typical ferrite (α = 0.05, ω_0 = 5, ω_m=1) (a), (b) Real and Imaginary parts of χ_{xx}, (c), (d) Real and Imaginary parts of χ_{xy}.

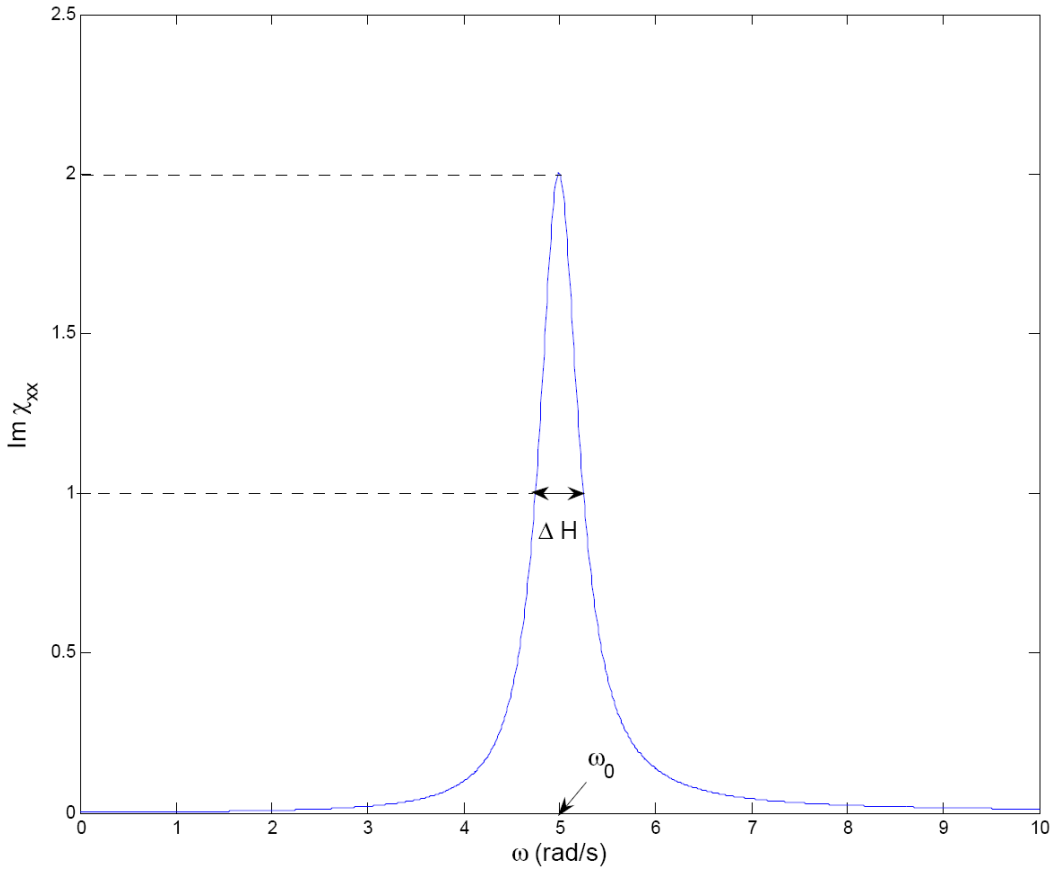

Figure 2.6 Definition of the linewidth ΔH, of the gyromagnetic resonance

2.4 Definition of S-parameter

The scattering matrix is a mathematical construct that quantifies how RF signals propagate through a multi-port network. This application is a way of specifying return loss and insertion loss. The most basic sense of S-parameters matrix refers to the ratio of voltage out versus voltage in. For an RF signal incident on one port, some fraction of the signal bounces back out of that port, some of it scatters and exits in other ports, and some of it disappears as heat or even electromagnetic radiation. In an N-port system, it contains N^2 coefficients (S-parameters) and each one representing a possible input-output path. S-parameters come in the *i* by *j* matrix [2.27], with the number of rows and columns equal to the number of ports. The matrix also can be written in [2.27] and a specific element of the [S] matrix can be determined as [2.28].

$$\begin{bmatrix} V_1^- \\ V_2^- \\ \vdots \\ V_{i-1}^- \\ V_i^- \end{bmatrix} = \begin{bmatrix} S_{11} & S_{12} & \cdots\cdots & S_{1(j-1)} & S_{1j} \\ S_{21} & S_{22} & \cdots\cdots & S_{2(j-1)} & S_{2j} \\ \vdots & \vdots & \ddots & \vdots & \vdots \\ S_{(i-1)1} & S_{(i-1)2} & \cdots\cdots & S_{(i-1)(j-1)} & S_{(i-1)j} \\ S_{i1} & S_{i2} & \cdots\cdots & S_{i(j-1)} & S_{ij} \end{bmatrix} \begin{bmatrix} V_1^+ \\ V_2^+ \\ \vdots \\ V_{j-1}^+ \\ V_j^+ \end{bmatrix} \quad [2.27]$$

$$S_{ij} = \frac{V_i^-}{V_j^+}\Big|_{V_k^+=0, k\neq j} \quad [2.28]$$

For the S-parameter subscripts "*ij*", "*j*" and "*i*" represent the input port and output port respectively. In this dissertation, the vector network analyzer only has two

ports. Thus the N-port model can be simply regarded as a two port model with a 2 by 2 matrix, shown in Figure 2.7.

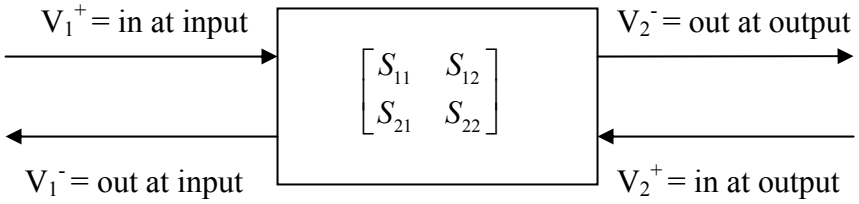

Figure 2.7 Diagram of a two-port network analyzer

Where, V_1^+ and V_2^+ are the voltage wave entering the port 1 and port 2 respectively; V_1^- and V_2^- are the voltage wave leaving the port 1 and port 2. The 2 by 2 matrix and each S parameter are defined in [2.29] and [2.30a ~ 2.30d].

$$\begin{bmatrix} V_1^- \\ V_2^- \end{bmatrix} = \begin{bmatrix} S_{11} & S_{12} \\ S_{21} & S_{22} \end{bmatrix} \begin{bmatrix} V_1^+ \\ V_2^+ \end{bmatrix} \quad [2.29]$$

$$S_{11} = \frac{V_1^-}{V_1^+},\ V_2^+ = 0 \quad [2.30a]$$

$$S_{12} = \frac{V_1^-}{V_2^+},\ V_1^+ = 0 \quad [2.30b]$$

$$S_{21} = \frac{V_2^-}{V_1^+},\ V_2^+ = 0 \quad [2.30c]$$

$$S_{22} = \frac{V_2^-}{V_2^+},\ V_1^+ = 0 \quad [2.30d]$$

Thus, S_{11} and S_{22} are called input reflection coefficient and output reflection coefficient respectively. Similarly, S_{21} is the electric field leaving the output divided by the electric field entering the input, when no signal enters the output.

Therefore, S_{21} is a transmission coefficient and is related to the insertion loss or the gain of the component. In like manner, S_{12} is a transmission coefficient related to the isolation of the component and specific how much power leaks back through the component in the wrong direction. It is concluded that parameters along the diagonal of the S-matrix are referred to as reflection coefficients because they only refer to what happens at a single port, while off-diagonal S-parameters are referred to as transmission coefficients, because they refer to what happens from one port to another.

S-parameter is in a complex form, including magnitude for the real part and phase change for the imaginary part. In order to quantify the change of voltage signal, the formula [2.31] of decibels (dB) is introduced to express relative differences in signal.

$$\mathrm{dB} = 20\log_{10}\left(\left|S_{ij}\right|\right) = 20\log_{10}\left(\sqrt{\left(\mathrm{Re}\left\{S_{ij}\right\}\right)^2 + \left(\mathrm{Im}\left\{S_{ij}\right\}\right)^2}\right) \qquad [2.31]$$

CHAPTER 3

Fabrication and Characterization of Ferrite Films

3.1 Thin Film Growth

The soft solution deposition (SSD) of ferrite thin film was developed by Massonori Abe and his colleague in 1983 [18-20]. He also named the soft solution deposition of ferrite as ferrite plating. Before that, the ferrite thin film was conventionally prepared at higher temperature (normally higher than 600^{o}C) by sputtering, vacuum evaporation, molecular beam epitaxy. These methods need to be operated under vacuum environment, unlike ferrite plating operated under atmosphere and low temperature (80-90^{o}C). The mechanism of ferrite plating proposed by Massonori Abe is shown in Figure 3.1. Initially, hydroxyl (OH^-) ions are adsorbed on the substrate and then release H^+ ions to react with the following Fe^{2+} ions to form bonding between O^{2-} and Fe^{2+}. Next part of the Fe^{2+} ions are oxidized to Fe^{3+} ions by an oxidation solution such as sodium nitrate ($NaNO_2$) solution. After Fe^{2+} ion adsorption and oxidization, hydroxyl (OH^-) ions adsorb on preadsorbed metal ions and this adsorption cycle is repeated by above sequence to continue the ferrite thin film growth. The reaction mechanism can be expressed by the following chemical reaction [3.1], [3.2]:

$$Fe^{2+} \rightarrow Fe^{3+} + e^{-} \qquad [3.1]$$

$$xFe^{2+} + yFe^{3+} + zM^{n+} + 4H_2O \rightarrow (Fe^{2+}Fe^{3+}M^{n+})_3O_4 + 8H^{+} \qquad [3.2]$$

where x + y + z = 1 and 2x + 3y + nz = 8.

The experiment setup is shown in Figure 3.2 to describe the ferrite plating by using spin-spray system. In this system, two reactive solutions including the metal ion sources containing $FeCl_2 \cdot 4H_2O$ (3g/L) (Aldrich) and $ZnCl_2$ (0~0.8g/L) (Fisher) aqueous solution, and the oxidation source containing an aqueous solution of $NaNO_2$ (0.5g/L) (Mallinckrodt) and CH_3COONH_4 (5g/L) (Alfa Aesar 97%) were sprayed continuously through the nozzle to the SiO_2 substrates at a flow rate of (50ml/min). Two nozzles were placed above the substrates in the rotating speed of 1000rpm. The substrates were heated to 80-90^{o}C by bottom heater and activated through a top halogen-lamp that is controlled by a transformer. A Halogen-lamp is used to irradiate the substrate with light and increase the deposition rate by 10 times than that without light. This method is called light-enhanced ferrite plating. The deposited film has a golden brown color, and the deposition rate is estimated about 0.2 μm/min from Jiqing Hu's dissertation [21].

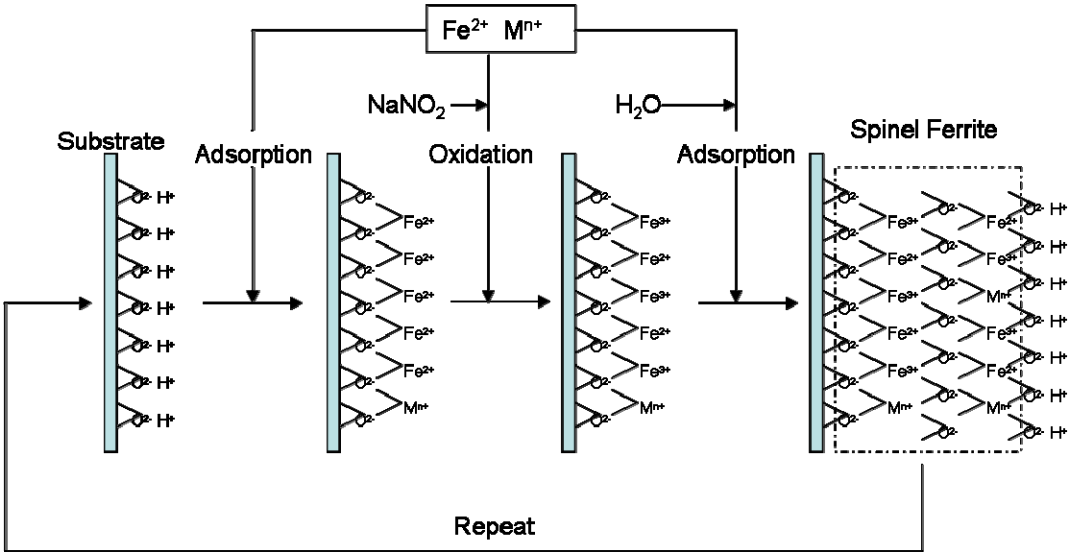

Figure 3.1 M. Abe's ferrite plating kinetic mechanism.

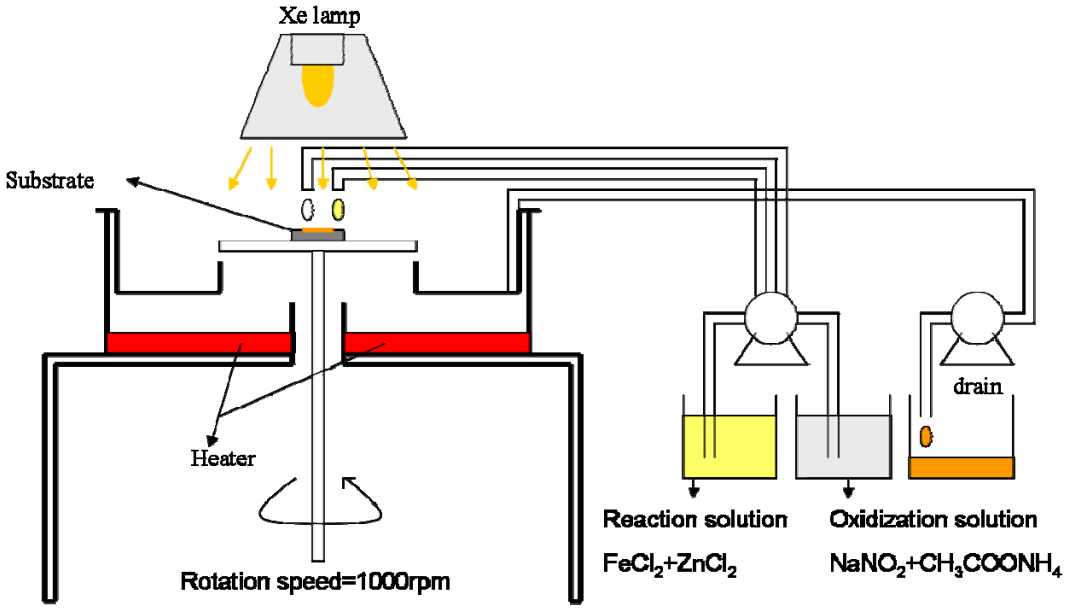

Figure 3.2 Schematic diagram of ferrite plating experimental setup.

3.2 Surface Characterization

Scanning Electron Microscope

The scanning electron microscope (SEM) is a type of electron microscope capable of producing high-resolution images of a sample surface. Due to the manner in which the image is created, SEM images have a characteristic three dimensional appearance and are useful for observing the surface structure of the sample. Figure 3.3(a), (b), and (c) show the SEM images of zinc ferrite thin films with deposition time during 15min, 45min and 75min respectively. It is observed that these films present round aggregates of small grains, and the aggregates grew larger with increasing deposition time. For the longest time (Figure 3.3(c)), the aggregates developed a cauliflower-like appearance. The higher magnification image shown in Figure 3.3(d) indicated the grains have a plate-like morphology with fibrous texture.

Contact Angle

Contact angle measurement is a good method for evaluating the surface wettability. The contact angle is given by Young's equation [3.3] and the diagram of force balance analysis on a liquid drop was shown in Figure 3.4 When the contact angle, θ, is between 90 and 180, the surface is hydrophobic to this liquid, otherwise when θ is between 0 and 90, the surface is hydrophilic. The film growth rate was determined by the thickness, which was measured by Veeco Dektak 8 profiler. It is shown by linear regression in Figure 3.5(a) that deposition rate is about 0.13 ~ 0.15μm/min. To observe the surface wetability phenomena, water

contact angle measurement was applied to all zinc ferrite films samples. Figure 3.5(b) shows the corresponding contact angle and root mean square roughness of zinc ferrite films on SiO_2 and Tantalum substrates in different thickness. For SiO_2 and Tantalum substrates, the water drop contact angle images of all zinc ferrite films in different thickness were shown in Figure 3.6(a) ~ (f) and Figure 3.7(a) ~ (e) respectively. It is observed from Figure 3.5(b) that the contact angle decreases with increasing film thickness, corresponding to the increasing roughness. It is easily understood that high surface roughness will cause the surface to be more hydrophilic, since the uneven surface can trap water molecules. Therefore, a drop of liquid can be quickly spread on the surface.

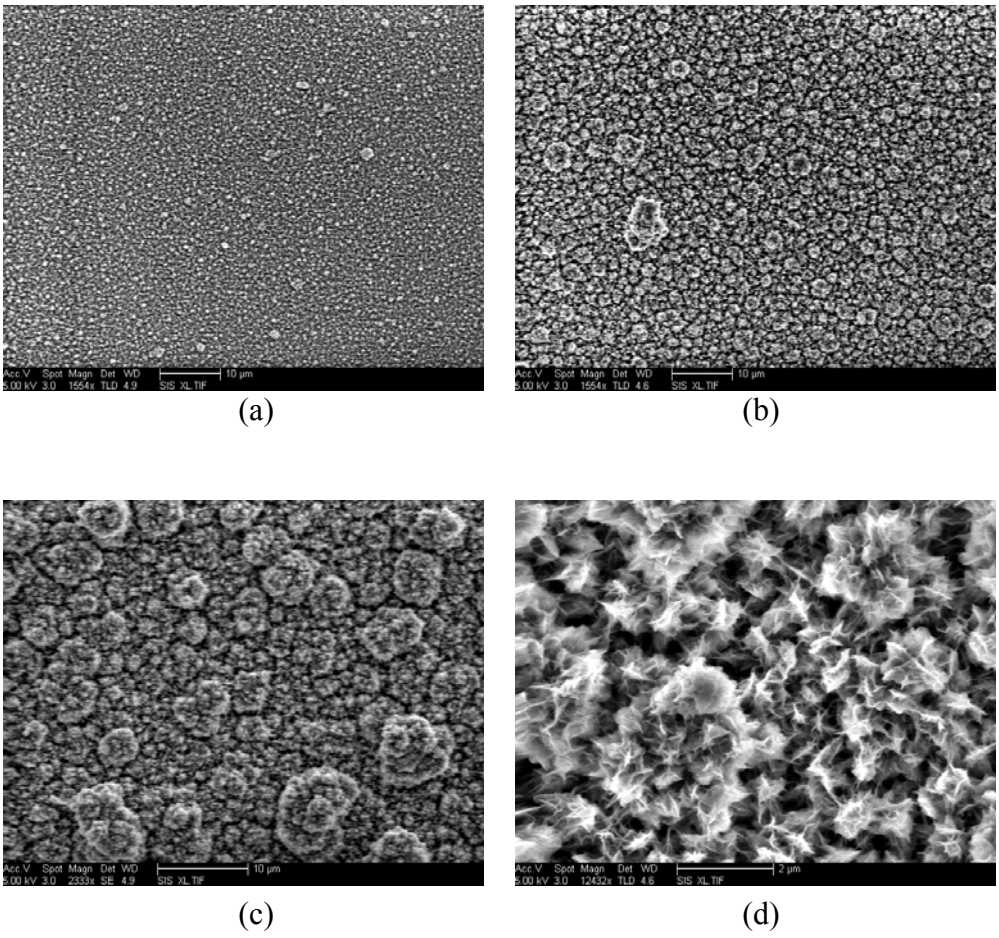

Figure 3.3 SEM images of plane-view structure of zinc ferrite thin films with different deposition time (a) 15 min. (b) 45 min. (c) 75 min. and (d) higher magnification image for (b) [Jiqing Hu, PhD Dissertation, OSU Library]

$$\gamma_{sg} = \gamma_{gl} \cos\theta + \gamma_{sl} \quad [3.3]$$

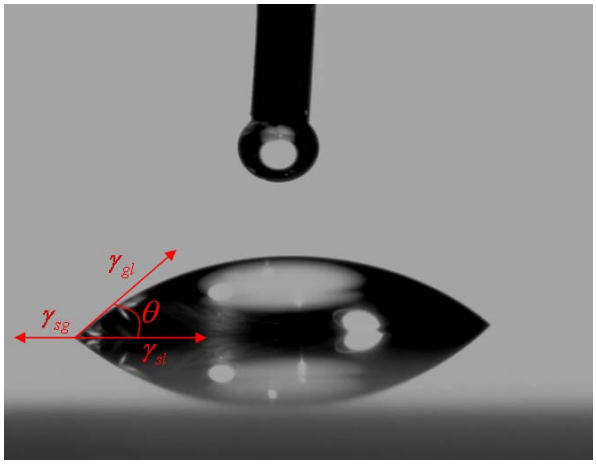

Figure 3.4 The diagram of force balance analysis on a liquid drop.

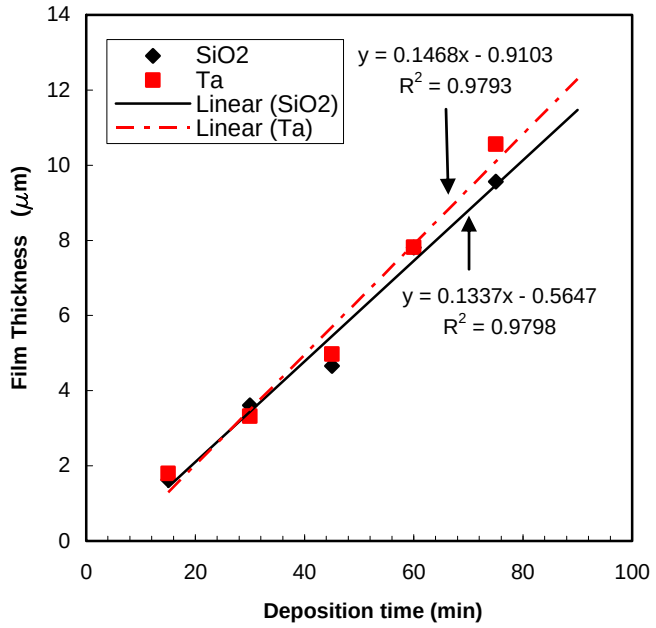

(a)

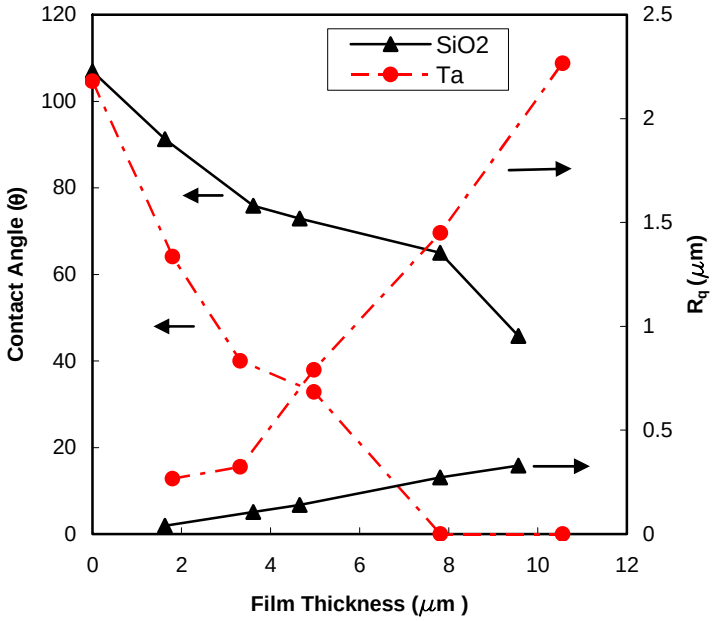

(b)

Figure 3.5 (a) Deposition time versus film thickness on different substrates, (b) Film thickness versus contact angle and surface roughness.

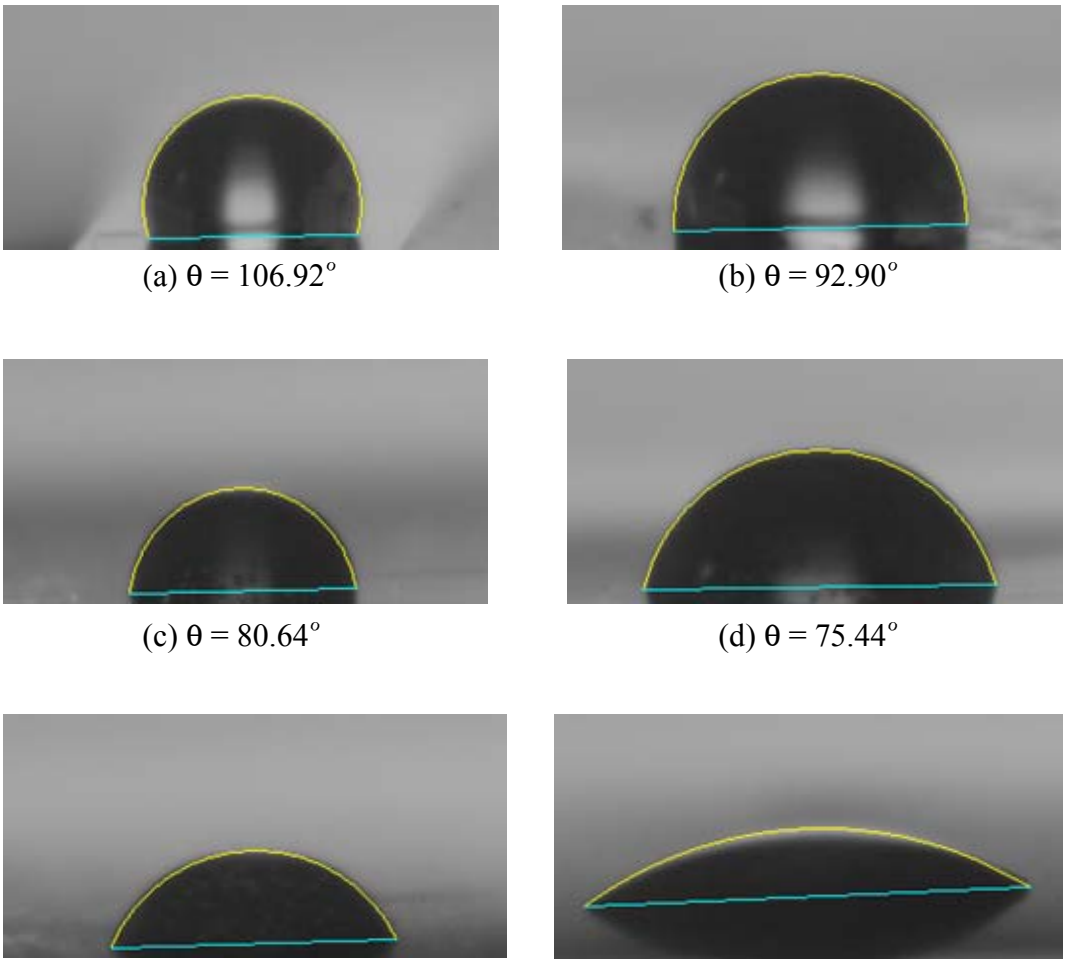

(a) θ = 106.92^o (b) θ = 92.90^o

(c) θ = 80.64^o (d) θ = 75.44^o

(e) θ = 66.43^o (f) θ = 33.85^o

Figure 3.6 Water contact angle on SiO_2 substrate with zinc ferrite film deposited during: (a) 0min, (b) 15min, (c) 30min, (d) 45min, (e) 60min, and (f) 75min.

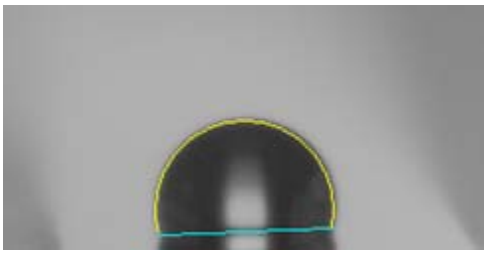

(a) θ = 104.61^o

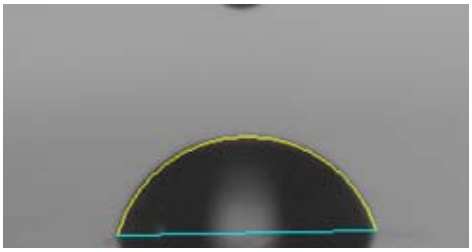

(b) θ = 73.51^o

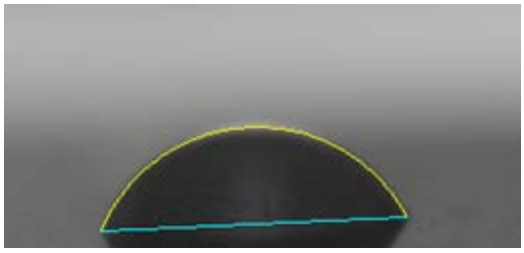

(c) θ = 65.13^o

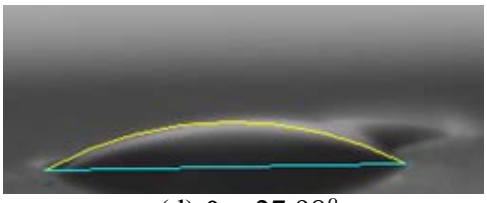

(d) θ = 27.98^o

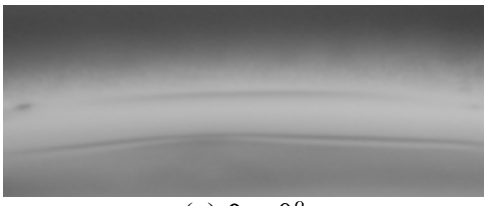

(e) θ = 0^o

Figure 3.7 Water contact angle on Tantalum substrate with zinc ferrite film deposited during: (a) 0min, (b) 15min, (c) 30min, (d) 45min, (e) 60min and 75min.

3.3 Film Fabrication

Screen Printing

Screen printing is a printmaking technique that traditionally creates a sharp-edged image by using a stencil and a porous fabric. In electronic industry, the screen-printing legend often refers to the writing on a printed circuit board (PCB). The printing technique may also be used in the process of etching copper wiring on the broad or IC (integrated circuit) chips. It is often preferred over other processes, such as dye sublimation or inkjet printing, due to its low cost and ability to print on many mediums.

The screen printing process, shown schematically in Figure 3.8, involves positioning the substrate on a carriage, which is then brought beneath the screen so that the substrate is in accurate region with the pattern on the screen. The substrate is placed in the printing position a short distance beneath the screen in order to have space for screen contacting with substrate. The pattern on the screen is fabricated by photolithographic technique so that the pattern can be printed through open areas to the substrate. A small amount of the paste is dispensed onto the upper surface of the screen. When a flexible wiper, called the squeegee, moves across the screen surface, the screen was brought to contact with the substrate and forces the paste through the open mesh areas. On removal of the squeegee, the screen regains its original position and leaves behind the printed paste pattern on the substrate. Finally, the process continues after the substrate is replaced from the carriage and removed from beneath the screen.

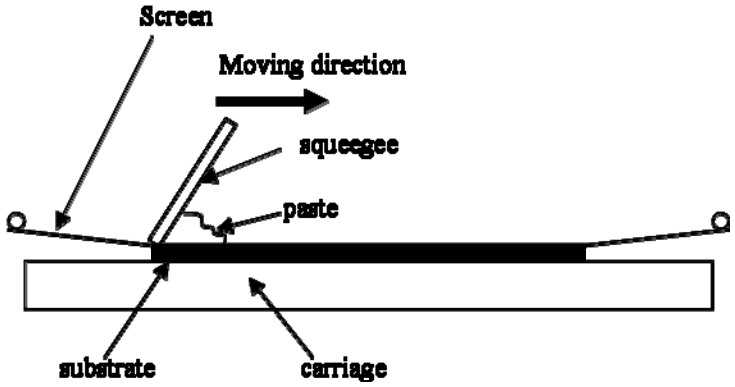

Figure 3.8 Schematic diagram of screen printing process.

The screen printing technique was used on fabricate YIG (yttrium iron garnet) thick film [22-24] Song et al.[22] prepared YIG powder by conventional ceramic processing and milled it with organic binder to obtain paste. Chen et al[23,24] applied the technique with hot-press sintering to print barium hexaferrite ($BaFe_{12}O_{19}$) films. The study includes the measurement of saturation magnetization and FMR (ferromagnetic resonance) linewidth (ΔH). Hot-press sintering process can produce dense thick film (100 ~ 500μm) with narrow line with, 320Oe. Therefore, barium hexaferrite prepared by this technique is believed to be the new generation of microwave device. The paste was used on screen printing to make YIG thick film .Thick film of YIG is well known as magnetic material for microwave device because of high saturation magnetization and low FMR (ferromagnetic resonance) line width (ΔH).

Pressure Die Casting

The pressure die casting fabrication is developed for replacing traditional screen printing fabrication. The purpose of pressure die casting is to apply external pressure for compressing powders more densely and fine, which is not achieved by screen printing. Actually, pressure die casting is using hot pressing to do the press procedure, but under room temperature. Some research may increase to high temperature for sintering powder or under vacuum environment. For this research, only pressure pressing is needed, because the sample is made by PCB broad which is not sustained to high temperature. Figure 3.9 shows the schematic diagram of pressure die casting fabrication. Before doing fabrication, an open area of 2mm *18mm is cut from a stainless sheet (5mil≃125μm in thickness) by Nd:YAG pulsed laser (ESI5330, 355nm wavelength). Place the stainless sheet mask on the testing device and match with the expected film area. Load the prepared YIG powders to the rectangular patch and place them in the chamber of the pressmaster vacuum hot press (HP30-4560, Thermal Technologies Inc). The external pressure is set up at 12.5lb/mm^2 to press the powders for few minutes. After that, releasing the load and stainless sheet mask, the densely magnetic film is formed.

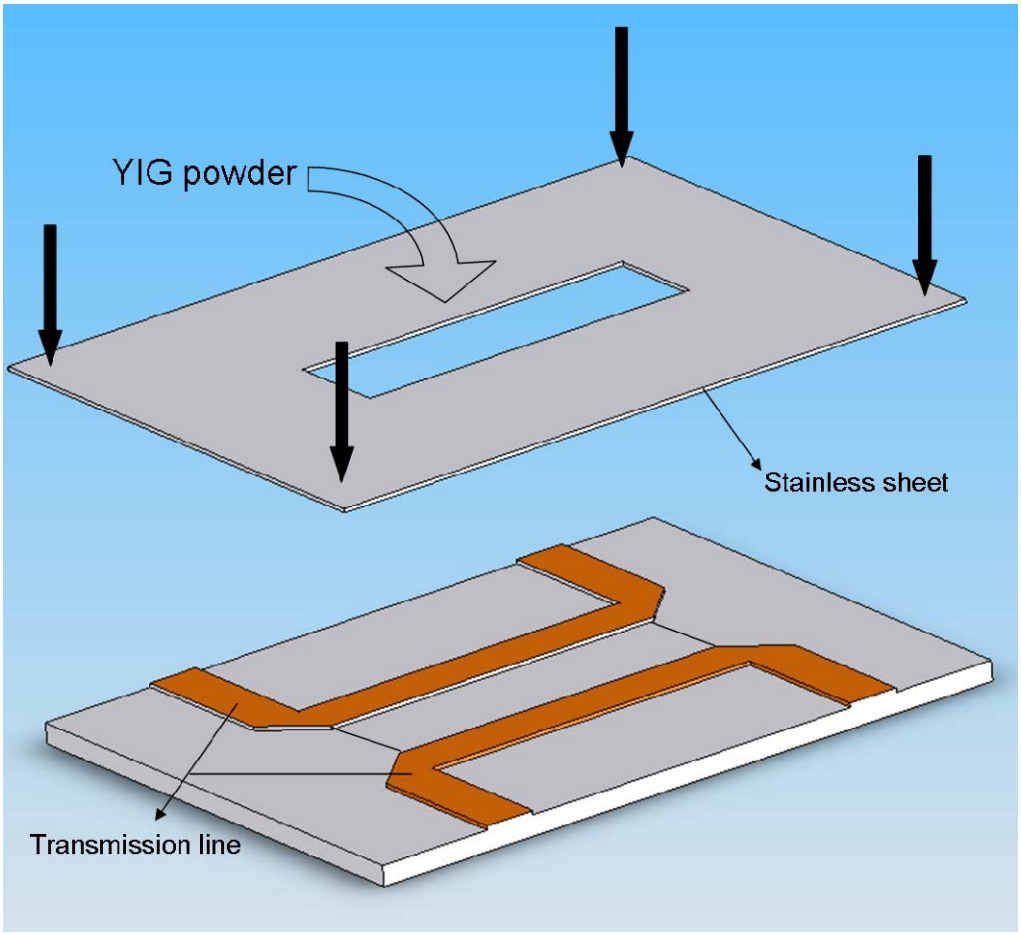

Figure 3.9 Schematic diagram of pressure die casting process.

CHAPTER 4

Crosstalk Suppression Measurement

4.1 Experiment

The disk shaped magnetic materials, yttrium iron garnet (YIG), were provided by Trans-Tech, Inc. By using a vibratory mill, disks were mixed with ethanol for grounding lasting 9 ~ 15 hours to get fine powder. After evaporating ethanol, the residual powder was collected from the flask. In this thesis, two kinds of methodology, screen printing (Chapter 3.3) and pressure pressing are applied for film fabrication. For screen printing, YIG powder was mixed with an organic adhesive and stirred for few seconds to form paste. The paste was spread on the area which is covered by a silk screen. The area is in the center of the device and between two strip transmission lines. After few minutes, removed the screen carefully and dried it for several hours. For pressure die casting, all procedures were following the Chapter 3.3 pressure pressing section (Figure 3.9).

4.2 Materials

The materials with high saturation magnetization and narrow line-widths are needed for this method of crosstalk suppression. In this dissertation, three materials YIG (G-113) and Calcium Vanadium substituted YIG (TTVG-1850, 1600) are used for crosstalk suppression. The material properties are listed in table 4.1.

Sample	Saturation Magnetization $4\pi Ms$ (G)	Dielectric Constant: ε_r	Remanent Induction: B_r (G)	Initial Permeability: μ_0
G113	1780	15	1277	134
TTVG1600	1600	14.6	1000	227
TTVG1850	1850	14.8	1232	388

Table 4.1 Magnetic properties of various YIG samples

4.3 S-parameters Measurement

A test structure shown in Figure 4.1 is fabricated on Roger Corp. RT/Duroid 5880 substrate (ε_r = 2.2, μ_r = 1, $\tan\delta$ =0.0004, substrate height = 0.031mm. S-parameter data is measured by using a Hewlett Packard 8722C vector network analyzer (VNA). Before measuring, certain frequency range need to be fixed and the calibration procedure is followed by the standard SOLT (short-open-load-through) method. The purpose of this method is to shift the reference plane to the 3.5 mm SMA connectors used to interface between the device and the VNA. The whole experiment setup is shown in Figure 4.2. The device is placed in the solenoid loop, which generate an external magnetic field (0.3~0.5G) by passing through a 2 Amp current. Then, two ports are connected to VNA wires and other 2 ports are connected to 50 ohms load. The measurement is run under the 70V and 2 Amp given by power supply (XFR 300-4). The near-end-crosstalk (NEXT) scattering parameter S_{31} is measured by port 1 and port 3, and far-end-crosstalk (FEXT) scattering parameter S_{41} is measured by port 1 and port 4.

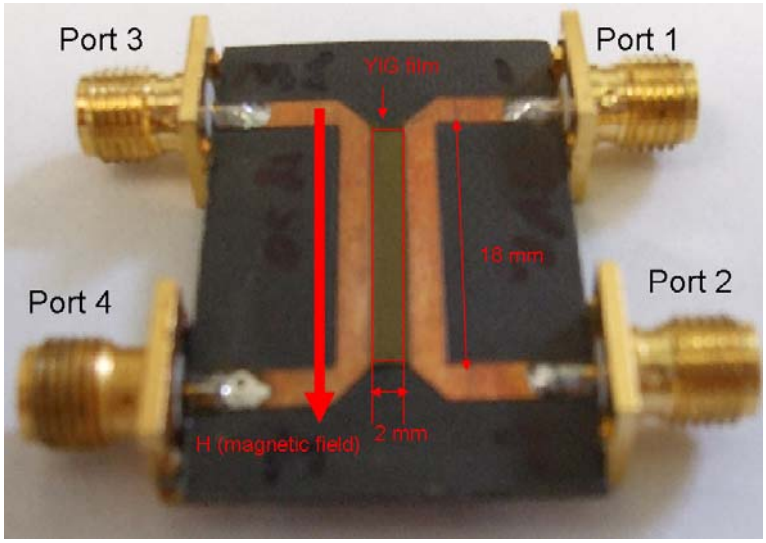

Figure 4.1 Test structure on PCB broad with YIG ferrite film

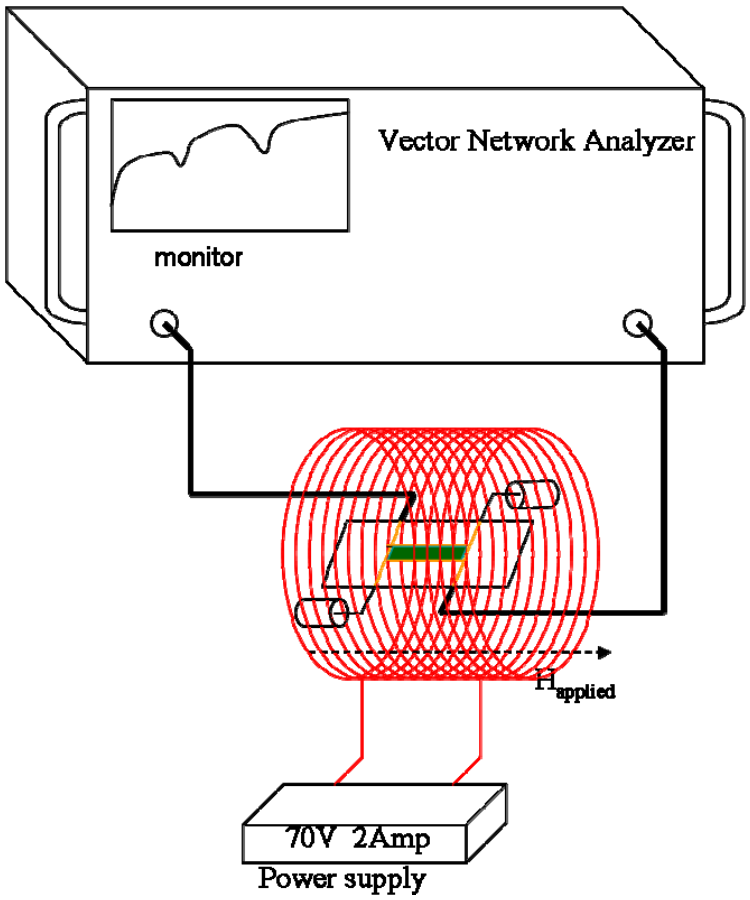

Figure 4.2 Device test of crosstalk measurement =

4.4 Measurement Result

Yttrium Iron Garnet: G-113

Figure 4.3 shows the near-end and far-end crosstalk for non-film device and the device with screen printed YIG: G-113 magnetic film. The magnetic film doesn't work efficiently for near-end crosstalk reduction, but for far-end crosstalk reduction with a change from -53dB to -63dB at a resonant frequency 0.75GHz. The predicted resonant frequency is 0.53GHz based on Kittel's equation [2.15~2.18]. The three dimensions of film are t = 40μm, L = 18mm, w = 2mm, and applied field, H_a = 0.5 Oe.

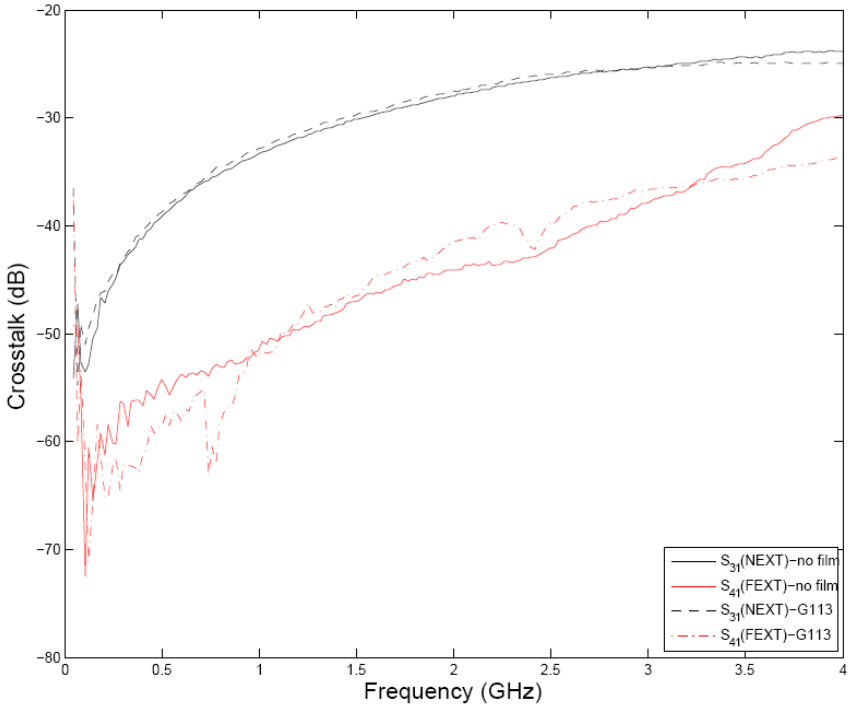

Figure 4.3 Near-end and far-end crosstalk for the test structure with no magnetic film and with YIG: G-113 magnetic film fabricated by screen printing.

Yttrium Iron Garnet: TTVG-1600

Figure 4.4 shows the near-end and far-end crosstalk for non-film device and the device with screen printed YIG: TTVG-1600 magnetic film. The result is similar to YIG: G-113 film, which has unapparent near-end crosstalk reduction but apparent far-end crosstalk reduction from -53dB to -65dB at a resonant frequency 0.63GHz. Also, the predicted resonant frequency is 0.42GHz, based on the three dimension of film are $t = 30\mu$m, $L = 18$mm, $w = 2$mm.

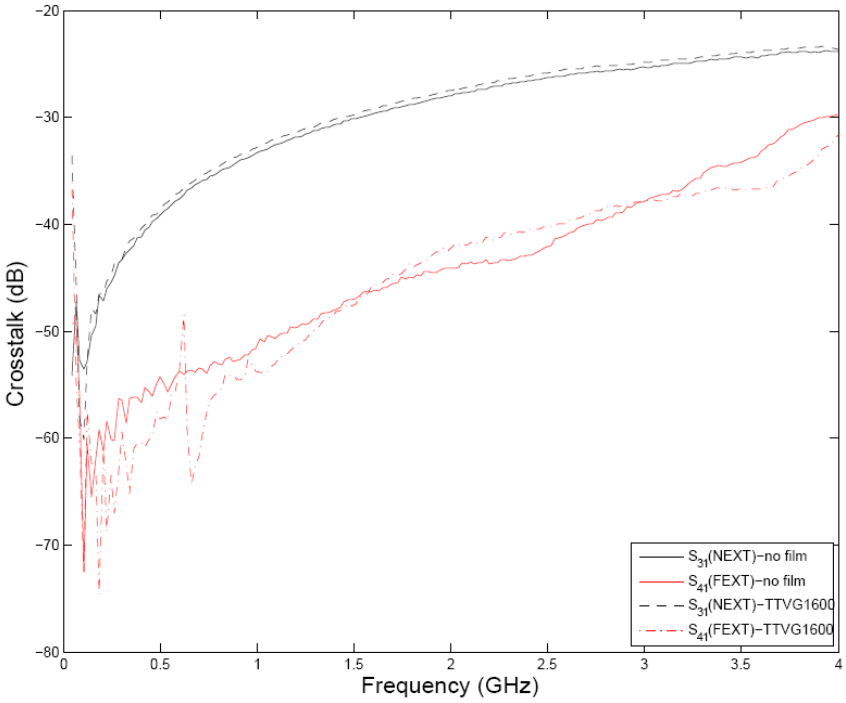

Figure 4.4 Near-end and far-end crosstalk for the test structure with no magnetic film and with YIG: G-1600 magnetic film fabricated by screen printing.

Yttrium Iron Garnet: TTVG-1850

Figure 4.5 shows the resulting far-end and near-end crosstalk for magnetic films fabricated by (a) screen printing and (b) pressure die casting under an applied field of H_a = 0.5 G. For screen printing technique, Figure 4.3(a) shows the crosstalk reduction is not apparent in the near-end, but significant improvement of 10dB in the far-end after 1GHz. The far-end crosstalk reduction has a change from -46dB to -57dB compared to non-film device. The resonant frequency is not clearly to distinguish at 1.7GHz, because of a small resonant peak. For pressure die casting technique, Figure 4.5(b) shows a dramatic reduction in far-end crosstalk from -50dB to -72dB and the resonant frequency occurs at 1.25GHz. The predicted resonant frequency is 0.57GHz based on Kittel's equation [2.15 ~ 2.18]. The three dimensions of film are t = 43μm, L = 18mm, w = 2mm, and applied field, H_a = 0.5Oe. Compared screen printing and pressure pressing, the later technique can make the film more densely and then get more improved crosstalk reduction.

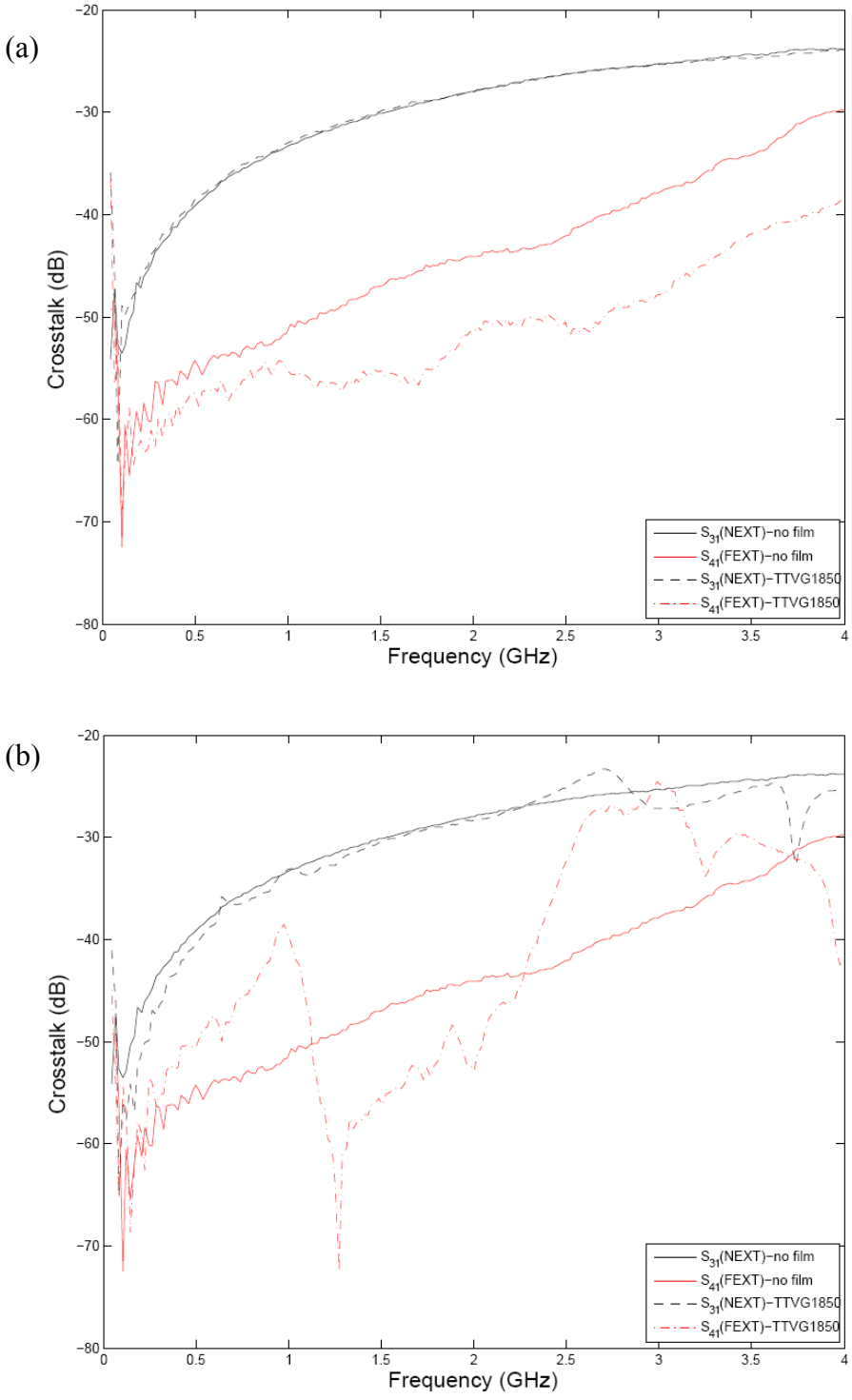

Figure 4.5 Near-end and far-end crosstalk for the test structure with no magnetic film and with YIG: G-1850 magnetic film fabricated by (a) screen printing (b) pressure die casting.

4.5 Discussion

Based on the result of Figure 4.3 ~ 4.5, it is concluded that using screen-printed YIG films result in far-end crosstalk suppression of 10 ~ 12dB, however, no suppression effect for near-end crosstalk. If the screen printing technique is replaced by pressure die casting, the far-end crosstalk can be further achieved by 22dB and the near-end crosstalk is also suppressed by 8dB at higher frequency 3.75GHz. The near-end crosstalk reduction is not discovered on screen-printed film device. It is suspected that the organic adhesive may have some influence preventing magnetic film reducing crosstalk. Therefore, the pressure die casting is superior to screen printing technique on film thickness control and fabrication.

CHAPTER 5

Conclusion and Future Work

5.1 Conclusion

The zinc ferrite was successfully deposited by ferrite plating method. TEM is used to characterize the nanoparticle crystalline. SEM and contact angle measurement are used to characterize surface morphology and wettability. Based on the result of Figure 4.3 ~ 4.5, it is concluded that using screen-printed YIG films result in far-end crosstalk suppression of 10 ~ 12dB, however, no suppression effect for near-end crosstalk. If the screen printing method is replaced by pressure die casting, the far-end crosstalk can be further achieved by 22dB and the near-end crosstalk is also suppressed by 8dB at higher frequency 3.75GHz.

5.2 Future Work

For the device test, the thickness of printed circuit broad needs to be measured without magnetic film after pressing, and then doing S-parameter measurement compared to the broad without pressing for making sure the pressing operation will affect the device performance or not. Because the substrate is made by soft polymer material, it may have deformation under very high pressure. If there was a substrate deformation, the distance from the ground plane to the microstrip would be lessened and this would cause the characteristic impedance of the microstrip to change. Along with changing how much coupling would occur in the directional coupler.

The future work should be focused on the fabrication process. A continuous flow reactor combined pressure die casting is proposed to synthesize nanoparticles. Here, the experiment setup of continuous flow reactor and preliminary result are showed in Figure 5.1 and Figure 5.2. The reaction system was consisting of peristaltic pump (Ismatec REGLO Digital), a 60cm Tygon tube (1.22mm I.D, Upchurch Scientific) and a T-mixer. The flow rate was set up at 1ml/min for each inlet and the Tygon tube was immersed in water bath keeping at 80-90°C. Few drops of mixing solution were dropped on lacy carbon film grid for transmission electron microscopy (TEM) characterization. The TEM image (Figure 5.3(a)) shows these nanoparticles with round shape 20 ~ 30nm in size. The selected area electron diffraction (SAED) presented in Figure 5.2(b) and d-value in Figure 5.2(c) further confirms the nanocrystalline structure of zinc ferrite ($ZnFe_2O_4$). These results indicate the occurrence of homogeneous particle formation in the micro channel.

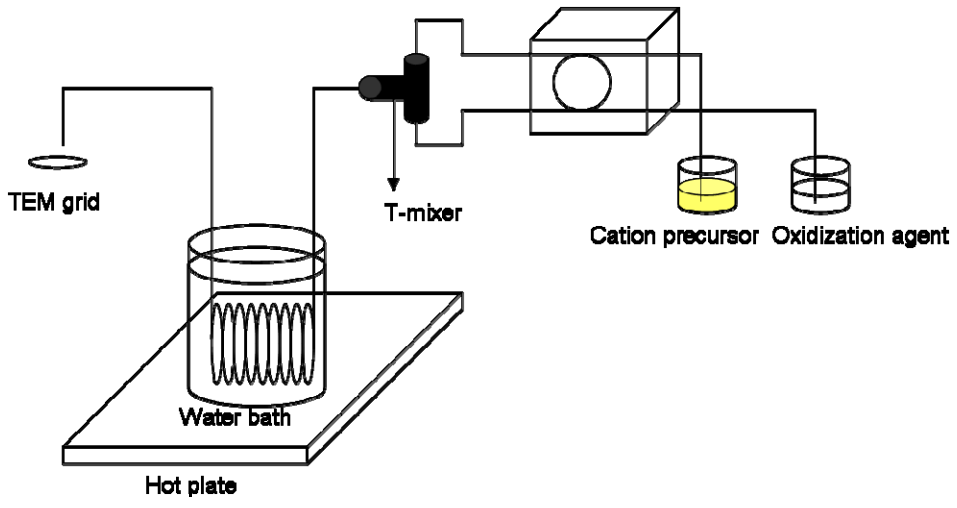

Figure 5.1 Schematic diagram of T-mixer mixing system.

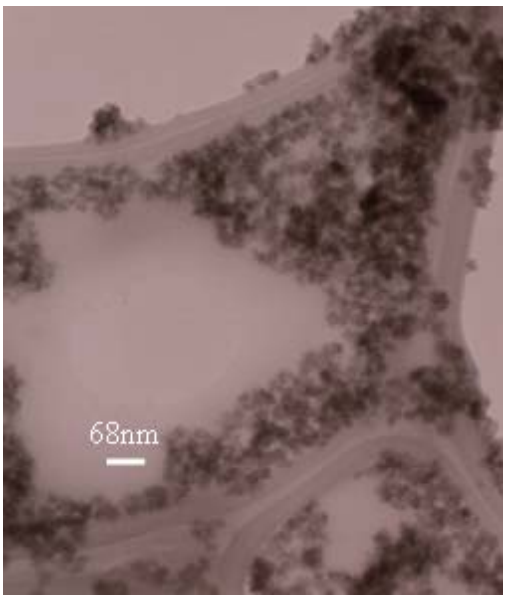

(a)

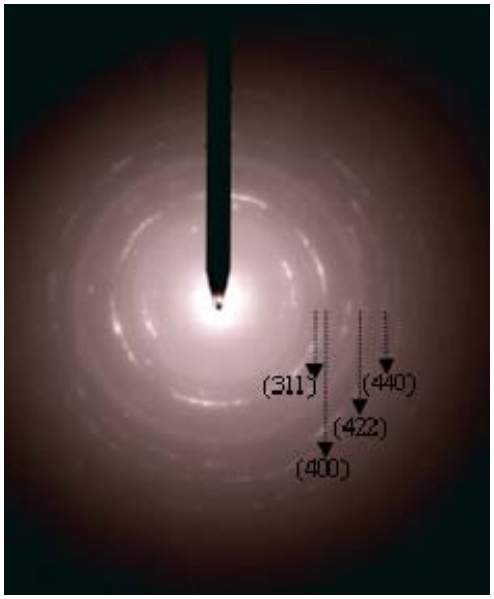

(b)

JCPDS (82-1049) $ZnFe_2O_4$ (Å)		Experiment (Å)
2.9843		------
2.5450	(311)	2.539
2.1102	(400)	2.243
1.9364		------
1.7229	(422)	1.693
1.4921	(440)	1.463
1.3346		------

(c)

Figure 5.2 Zinc ferrite ($ZnFe_2O_4$) (a) TEM image, (b) SAED pattern, (c) d-value from SAED pattern.

XRD Characterizations

X-ray diffraction (XRD) is a powerful non-destructive technique to characterize the crystalline orientation in the sample of powder or thin film. The micro-reactor system was again introduced to depositing thin film. In Figure 5.2, only the TEM lacy carbon grid was changed to a SiO_2 substrate on a hot plate, and halogen-lamp was on top of the substrate. All other operation parameters, such as flow rate and length of tubes are the same. The deposition time is lasted for 10 min. Zinc ferrite and yttrium iron oxide thin film was deposited for XRD characterization.

To deposit zinc ferrite thin film, the precursors of cation solution was composed of $FeCl_2 \cdot 4H_2O$ (0.015M) and $ZnCl_2$ (0.0015M), and the oxidation solution contains $NaNO_2$ (0.0073M) and CH_3COONH_4 (0.065M). Figure 3.9 shows the XRD patterns for (b) as-deposited and (c) annealed in 1000ºC compared to data base file (a) JCPDS 82-1049. The "circle" symbol in Figure 5.3 represents the crystalline orientation of SiO_2 substrate, and the "star" symbol represents $ZnFe_2O_4$ thin film. Two peaks of (c) 1000 ºC annealed samples occurs at 29.99^o and 35.384^o, which are close to peaks at 29.917^o and 35.236^o of (a) JCPDS 44-1067. The corresponding orientation are (3 1 1) and (2 2 2) respectively.

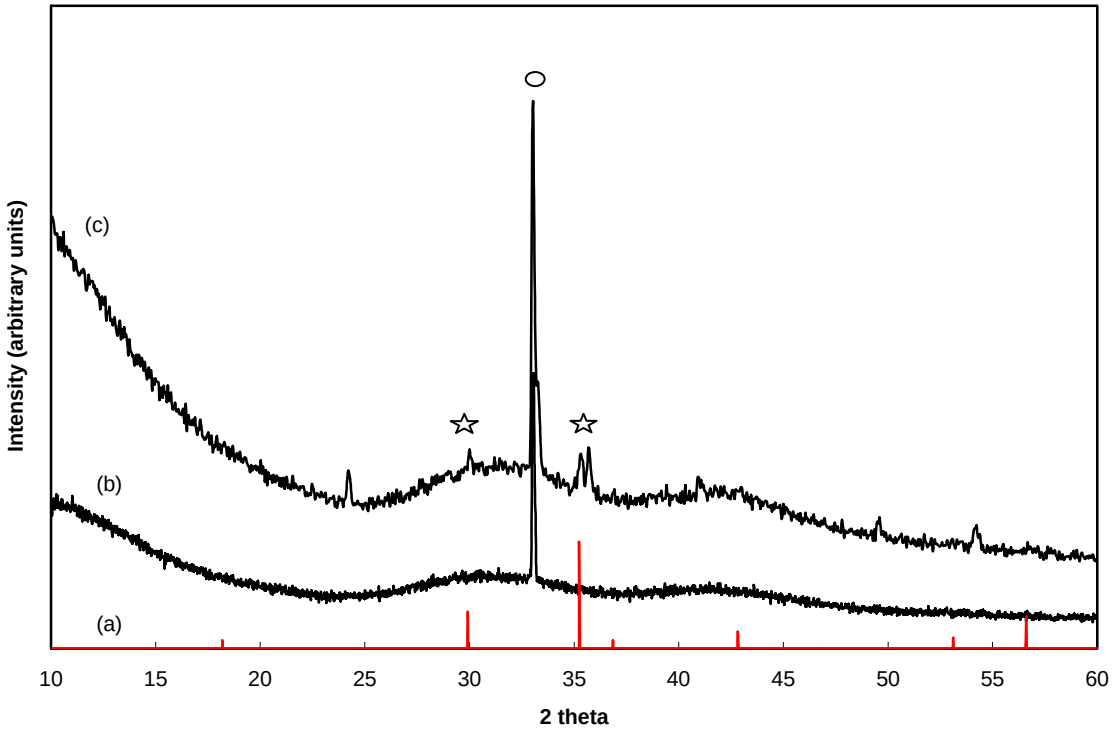

Figure 5.3 X-ray diffraction patterns of $ZnFe_2O_4$: (a) JCPDS 82-1049 ($ZnFe_2O_4$), (b) as-deposited, (c) annealed in 1000 ºC

To deposit yittrium iron oxide thin film, the precursors of cation solution were composed of $FeCl_2 \cdot 4H_2O$ (0.015M) and YCl_3 (0.009M) The oxidation solution contained $NaNO_2$ (0.0073M) and CH_3COONH_4 (0.065M). Figure 5.4 shows the XRD pattern for (b) as-deposited and (c) annealed in 400 ºC compared to data base file (a) JCPDS 44-1067. The "circle" symbol in Figure 3.10 represents the crystalline orientation of SiO_2 substrate, and the "star" symbol represents $Y_2Fe_4O_9$ thin film. Two main peaks of (b) as-deposited and (c) annealed samples occurs at 36.64^o and 43.02^o, which are close to peaks at 36.297^o and 43.872^o of (a) JCPDS 44-1067. The corresponding orientation are (1 0 2) and (1 0 3) respectively. The commercial yttrium iron garnet ($Y_3Fe_5O_{12}$) from Trans-Tech Inc. was also characterized by XRD. Figure 5.5 shows the diffraction pattern for (b) G113 (Aluminum and Gadolinium doped) and (c) TTVG1950 (Calcium and Vanadium doped). It is indicated that every peak of G-113 and TTVG-1850 are exactly match with JCPDS 77-1988. The main peak of G-113 and TTVG-1850 occurs at $2\theta = 32.38^o$ and 32.3^o respectively, with corresponding crystal orientation at (4 2 0).

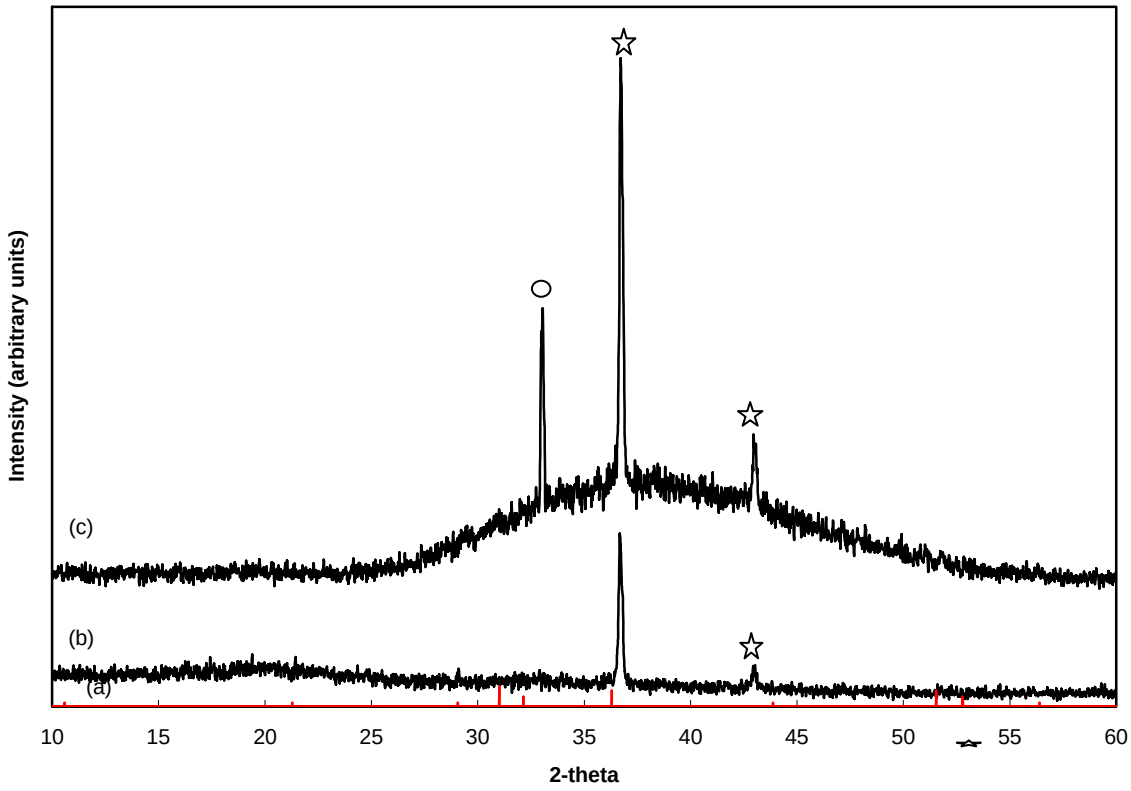

Figure 5.4 X-ray diffraction patterns of $Y_2Fe_4O_9$: (a) JCPDS 44-1067 ($Y_2Fe_4O_9$), (b) as deposited, (c) annealed in 1000 ºC

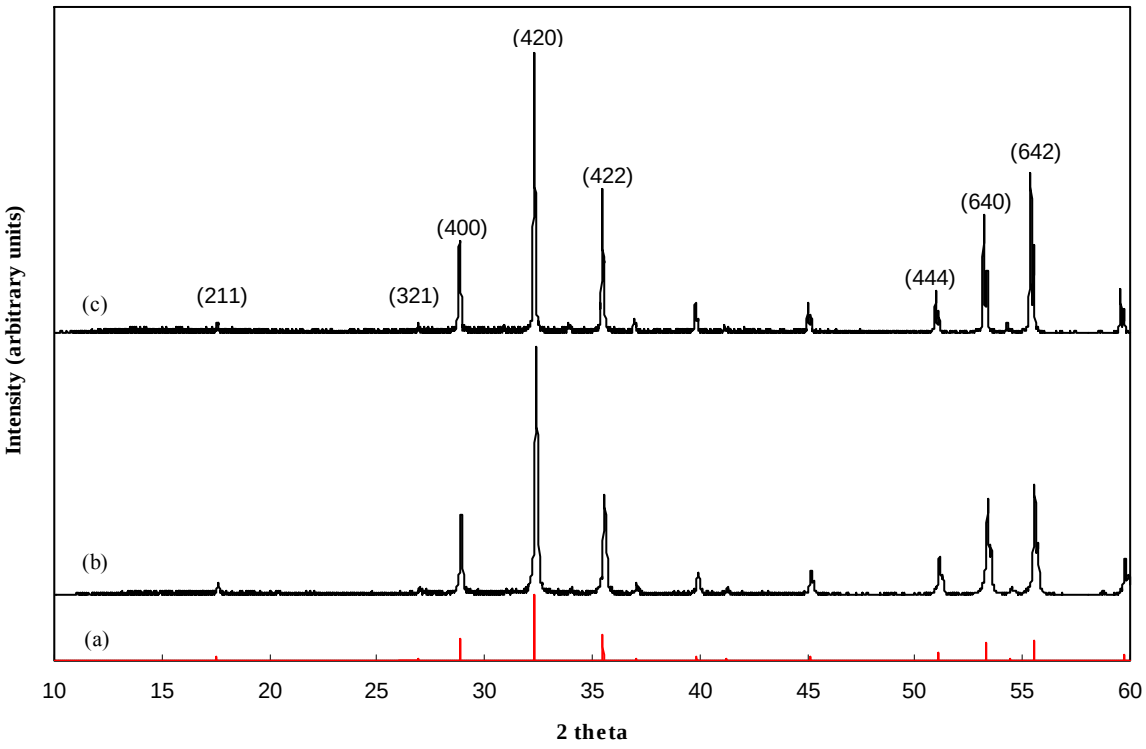

Figure 5.5 X-ray diffraction patterns of $Y_3Fe_5O_{12}$: (a) JCPDS 77-1988 ($Y_3Fe_5O_{12}$), (b) YIG garnet G-113, (c) YIG garnet TTVG-1850

References

[1]. D. G. Kam, H. Lee, J. Kim, J. Kim, "*A New Differential Line Structure on High- Speed Printed Circuit Broads to Enhance Immunity to Crosstalk and External Noise*", IEEE microwave and wireless components letters, vol. 13, No 9, 2003.

[2]. J. Gipprich, D. Stevens, "*A new via fence structure for crosstalk reduction in high density stripline packages*", Microwave Symposium Digest, 2001 IEEE MTT-S, International, Vol.3, 2001, pp. 1719-1722.

[3]. J.P.K. Gilb, C. A. Balanis, "*Coupling reduction in high-speed, high-density digital interconnects with substrate compensation*", Electrical Performance of Electronic Packaging, April 1992 pp. 116. 118.

[4]. M. Yamaguchi, K. H. Kim, T. Kuribara, K.-I. Arai, "*Thin-Film RF Noise Suppressor Integrated in a Transmission Line*", IEEE Trans. Magn., vol.38, No.5, p3183 (2002)

[5]. K. H. Kim, M. Yamaguchi, S. Ikeda, K.-I. Arai, "*Modeling for RF Noise Suppressor Using a Magnetic Film on Coplanar Transmission Line*", IEEE Trans. Magn., vol.39, No.5, p3031 (2003)

[6]. K. H. Kim, S. Bae, M. Yamaguchi, "*Dimensional Effects of the Magnetic Film on Coplanar Transmission Line for RF Noise Suppression*", IEEE Trans. Magn., vol.40, No.4, p2847 (2004)

[7]. S. Ohnuma, H. Nagura, H. Fujimori, T. Masumoto, "*Noise Suppression Effect of Nanogranular*", IEEE Trans. Magn., vol.40, No.4, p2712 (2004)

[8]. K. H. Kim, M. Yamaguchi, K.-I. Arai,"*Effect of radio-frequency noise suppression on the coplanar transmission line using soft magnetic thin films*", J. Appl. Phys. Vol.93, No.10, p8002 (2003)

[9]. K. H. Kim, S. Ikeda, M. Yamaguchi, K.-I. Arai, "*FEM analysis on the effects of soft magnetic film as a noise suppressor at GHz range*", J. Appl. Phys. Vol.93, No.10, p8588 (2003)

[10]. K. H. Kim, M. Yamaguchi, "*Microwave absorption of integrated CoNbZr film on a coplanar waveguide*", J. Appl. Phys. vol.99, 08M902 (2006)

[11]. K. H. Kim, M. Yamaguchi, S. Ikeda, K.-I. Arai, "*Modeling for RF Noise Suppressor Using a Magnetic Film on Coplanar Transmission Line*", IEEE Trans. Magn., vol.39, No.5, p3031 (2003)

[12]. K. H. Kim, S. Bae, M. Yamaguchi, "*Dimensional Effects of the Magnetic Film on Coplanar Transmission Line for RF Noise Suppression*", IEEE Trans. Magn., vol.40, No.4, p2847 (2004)

[13]. K. H. Kim, M. Yamaguchi, K.-I. Arai, "*Effect of radio-frequency noise suppression on the coplanar transmission line using soft magnetic thin films*", J. Appl. Phys. Vol.93, No.10, p8002 (2003)

[14]. Rolf E. Hummel, "Electronic Properties of Materials", Springer 2001

[15]. Arien Sligar, Dissertation: "On-Chip Crosstalk Suppression Schemes Using Magnetic Films for RF/Microwave Application"

[16]. Charles Kittel, "*On the theory of ferromagnetic resonance absorption*", phys. Rev. vol 73, 2, 155 (1948)

[17]. David M. Pozar, chapter 4.3, "Microwave Engineering", John Wiley & Sons, Inc. 2005

[18]. Masanori Abe, "*A soft solution processing technique for preparing ferrite films and their applications*", MRS Bulletin/September 2000

[19]. Tomoyuki Itoh, Masanori Abe, Yutaka Tamaura, "*Ferrite plating of $(Fe,Ni,Zn)_3O_4$ films in aqueous solution by an improved spray-spin-coating method* ", Jpn. J. of Appl. Phys. Vol.27, No.5, 839 (1988)

[20]. T. Itoh, S. Hori, M. Abe, Y. Tamaura, "*Light-enhanced ferrite plating of $Fe_{3-x}M_xO_4$ (M= Ni, Zn, Co, and Mn) films in an aqueous solution*", J. Appl. Phys. 69(8), 5911 (1991)

[21]. Jiqing Hu, dissertation "*Growth and Characterization of Zinc Ferrite Thin Films for High Frequency Applications*", Oregon State University library 2006

[22]. Hang-Kyu Song, J. H. Oh, J. C. Lee, S. C, Choi, "*Magnetic Properties and Microstructure of YIG thick films prepared by screen printing*", phys. Stat. Sol. (a)189, No. 3, 829-832(2002)

[23]. Y. Chen, A. L Geiler, T. Sakai, S.D. Yoon, C. Vittoria, V. G. Harris, "*Microwave and magnetic properties of self-biased barium hexaferrite screen printed thick films*", J. Appl. Phys. 99, 08M904 (2006)

[24]. Y. Chen, T. Sakai, T. Chen, S.D. Yoon, C. Vittoria, V. G. Harris, " *Screen printed thick self-biased, low-loss, barium hexaferrite films by hot-press sintering*",J. Appl. Phys. 100, 043907 (2006)

Appendix A

γ is the gyromagnetic ratio. It is defined as the ratio of magnetic dipole moment [A.1] and spin angular momentum [A.2].

$$m = \frac{q\hbar}{2m_e} = 9.27*10^{-27} \text{ A-m}^2 \qquad [A.1]$$

$$s = \frac{\hbar}{2} \qquad [A.2]$$

m_e is the mass of the electron, q is the electro charge, and $\hbar$ is Planck's constant divided by 2π. Thus, γ is given by

$$\gamma = \frac{m}{s} = \frac{q}{m_e} = 1.759*10^{11} \text{ C/Kg} \qquad [A.3]$$

For practical usage in [2.14], γ with SI units should be converted to typical value with the commonly used magnetic c.g.s unit system. The derivation is presented in [A.4]

$$\begin{aligned} \gamma/2\pi &= 1.759*10^{11}/2\pi \text{ [C/Kg]} \\ &= 2.8*10^{10} \text{ [(C·s)/(Kg·s)]} \\ &= 2.8*10^{10} \text{ [(1/s)/(Kg/(s·C))]} \\ &= 2.8*10^{10} \text{ [Hz/T]} \\ &= 2.8*10^{10} \text{ [Hz/}10^4 \text{ G]} \\ &= 2.8 \text{ [MHz/ Oe]} \end{aligned} \qquad [A.4]$$